Eksplorium *p*-ISSN 0854-1418
Volume 47 No. 1, January 2026: 64–92 *e*-ISSN 2503-426X

Label-Free Electrochemical Biosensor Based on Electrospun rGO/Ag/PANI Nanofibers for Sensitive Detection of HER2-Positive Breast Cancer Cells

Sara Bahrami[1], Amir Amirabadi[2], Laleh Maleknia[3]* and Hassan Tavakoli[4]

[1]Department of Biomedical Engineering, ST.C., Islamic Azad University, Tehran, Iran

Email: 1271266520@iau.ir

[2]Department of Biomedical Engineering, ST.C., Islamic Azad University, Tehran, Iran,

Email: a_amirabadi@azad.ac.ir

[3]Department of Biomedical Engineering, ST.C., Islamic Azad University, Tehran, Iran

*Corresponding Author: **Laleh Maleknia** Email: Malekniamood@iau.ac.ir

[4]Department of Physiology and Biophysics, Faculty of Medicine, Baghiatellah University of Medical Science, Tehran, Iran

Email: tavakoli@iau.ac.ir

Article Received: 02 December 2025, Revised: 10 January 2026, Accepted: 22 January 2026

ABSTRACT

In this work, we present the development of a novel label-free electrochemical biosensor based on electrospun nanofibers composed of reduced graphene oxide (rGO), silver nanoparticles (AgNPs), and polyaniline (PANI) for the sensitive detection of HER2-overexpressing breast cancer cells. The rGO/Ag/PANI nanofibers were deposited onto a glassy carbon electrode (GCE), providing a highly conductive and biocompatible interface with a large surface area for antibody immobilization and efficient electron transfer. The sensor demonstrated a wide linear detection range from 10 to 10^6 *cells/mL* and achieved an impressively low detection limit of 2 *cells/mL* for SK-BR3 cells (a HER2-positive breast cancer cell line), without the need for chemical labeling or signal amplification. The platform also showed high selectivity toward HER2-positive cells compared to HER2-negative controls. Recovery experiments in artificially spiked blood samples indicated >90% recovery, highlighting the sensor's robustness in complex biological environments under controlled in vitro conditions. Overall, the rGO/Ag/PANI-based nanofiber biosensor offers an effective strategy for rapid, label-free detection of target cancer cells in laboratory settings, and holds potential for further adaptation toward non-invasive diagnostic platforms following future clinical validation.

Keywords: Breast Cancer; Electrochemical Nano Biosensor, Impedance, Human Epidermal Growth Factor Receptor 2 (HER2), Graphene Oxide, Silver Nanoparticles.

1. INTRODUCTION

Breast cancer (BC) is one of the most prevalent and deadly malignancies among women worldwide, accounting for significant morbidity and mortality each year [1]. Among its molecular subtypes, approximately 20–30% of invasive breast cancers are characterized by overexpression or amplification of the human epidermal growth factor receptor 2 (HER2), a member of the ErbB tyrosine kinase receptor family [11–15]. HER2 overexpression is strongly correlated with increased tumor aggressiveness, recurrence rates, and resistance to conventional therapies [16]. Clinically, the extracellular domain (ECD) of HER2 can be cleaved and released into the bloodstream, serving as a valuable biomarker for non-invasive diagnostics and disease monitoring.

Current clinical methods for HER2 detection—such as immunohistochemistry (IHC) and fluorescence in situ hybridization (FISH)—are considered diagnostic gold standards but are invasive, time-consuming, and vulnerable

to false results due to tumor heterogeneity, subjective interpretation, and sampling limitations [11–13,17]. These drawbacks make them unsuitable for repeated monitoring or use in point-of-care (POC) settings, particularly in low-resource environments. Additionally, the specificity of HER2 expression to a subset of BC patients necessitates detection strategies that are both highly selective and minimally invasive.

To overcome these limitations, numerous electrochemical biosensors have been developed in recent years for HER2 detection. These platforms leverage redox-active interfaces to convert antigen–antibody interactions into measurable electrical signals, offering advantages such as high sensitivity, portability, and real-time readout [2,20,21]. For example, Freitas et al. developed a quantum dot-labeled electrochemical immunosensor achieving sub-nanomolar sensitivity in serum, though requiring complex labeling and multistep processing [2]. Similarly, impedance-based HER2 sensors have demonstrated promising sensitivity but often function only in buffer solutions or require immobilization of labeled antibodies, limiting their clinical applicability [21,23]. Most existing studies also detect recombinant HER2-ECD rather than whole HER2-positive cells, which may be more clinically relevant for tracking circulating tumor cells (CTCs) in metastatic disease.

Recent advances (2024–2025) in device-centric HER2 biosensors have greatly expanded the analytical landscape across multiple transduction modalities. Electrochemical platforms have achieved sub-nanomolar sensitivity through hybrid nanostructures and aptamer-functionalized interfaces [111–113]. Field-effect transistor (FET) and organic thin-film transistor (OTFT) devices now enable label-free, real-time HER2 detection with miniaturized, on-chip readout capabilities [114–116]. Plasmonic and surface acoustic wave (SAW) biosensors have further enhanced optical and mass-based responses for HER2 recognition [117,118]. Nevertheless, most of these recent devices target the soluble HER2 extracellular domain (HER2-ECD) in buffer or diluted serum and still rely on labeling or sample pretreatment. In contrast, the present study introduces a label-free electrochemical biosensor capable of directly detecting intact HER2-overexpressing breast cancer cells in untreated whole blood, thereby addressing the main limitations of current device-based HER2 sensing platforms.

From a device-engineering standpoint, the present work introduces a hierarchical rGO/Ag/PANI nanofiber-modified GCE that integrates three synergistic design features rarely combined in HER2 sensing devices: (i) a highly conductive hybrid nanofiber scaffold enabling efficient charge transport, (ii) label-free impedance transduction allowing direct whole-cell detection, and (iii) compatibility with untreated whole blood, eliminating the need for centrifugation or chemical processing. Unlike previous HER2 devices that primarily target the soluble HER2-ECD using labeled assays or high-cost transducers, our platform combines low-cost fabrication, scalable electrospinning, robust 60-day stability, and potential for miniaturization into portable point-of-care systems.

To the best of our knowledge, no existing electrochemical biosensor platform has successfully combined label-free operation, direct whole blood analysis, and ultrasensitive detection of intact HER2-positive breast cancer cells. This study addresses this gap by developing a hierarchical nanocomposite-modified glassy carbon electrode (GCE), functionalized with reduced graphene oxide (rGO), silver nanoparticles (AgNPs), and polyaniline (PANI) nanofibers. The synergistic integration of these components provides a conductive, high-surface-area, and biocompatible interface that facilitates antibody immobilization and enhances signal transduction [25–27].

The resulting biosensor exhibits a remarkably low detection limit (2 cells/mL), high selectivity against common interferents, and over 90% recovery efficiency in untreated whole blood samples—without requiring any sample preprocessing or external labeling. This unique combination of features clearly distinguishes our approach from previous work and positions it as a promising platform for point-of-care diagnostics and personalized monitoring in HER2-positive breast cancer patients.

2. MATERIALS AND METHODS

2.1. Materials

Silver nanoparticles (Ag, 99.99% purity, average diameter ~20 *nm*, metal basis) and graphene oxide nanoparticles (GO, 99% purity, lateral size 2–7 *nm*, comprising 6–10 layers) were both procured from US Research Nanomaterials Co. Sodium borohydride ($Na[BH_4]$), dimethylformamide (DMF), potassium dihydrogen phosphate

(KH_2PO_4), and dipotassium hydrogen phosphate (K_2HPO_4) salts were obtained from Merck (Germany). Polyacrylonitrile copolymer, consisting of 93.7% acrylonitrile and 6.3% vinyl acetate with a molecular weight of approximately 100,000 *g/mol*, was supplied by Isfahan Polyacryl Inc., Iran. Monoclonal anti-HER2 antibodies (AHAb) were purchased from Sigma-Aldrich (USA). The human breast cancer cell line SK-BR-3 was obtained from the American Type Culture Collection (ATCC).

2.2. Preparation of (rGO)

Initially, 0.1 *g* of graphene oxide (GO) was dispersed in 50 *mL* of deionized water under vigorous stirring at 120 *°C*. Then, a freshly prepared aqueous solution of sodium borohydride ($Na[BH_4]$) was added gradually to the suspension over a period of 45 *min* to ensure controlled reduction. The exact concentration and volume of the $Na[BH_4]$ solution were carefully measured prior to addition. After completion of the reduction reaction, the mixture was cooled to room temperature and neutralized by careful addition of dilute acid (e.g., diluted HCl) to adjust the pH to neutral, preventing undesired side reactions. The reduced graphene oxide (rGO) product was then collected via centrifugation, washed multiple times with deionized water to remove residual reagents and by-products, and finally dried under vacuum at 50 *°C* to remove moisture.

2.3. Preparation of rGO/Ag Nanocomposite

A total of 0.2 *g* of reduced graphene oxide (rGO) was dispersed in 20 *mL* of dimethylformamide (DMF) using a heater-stirrer setup under vigorous stirring for 30 *min* to ensure complete dispersion. Subsequently, predetermined amounts of silver nanoparticles (Ag) corresponding to 1%, 2%, 3%, and 4% weight ratios relative to rGO were separately added to 5 *mL* aliquots of the rGO dispersion. To promote uniform distribution and prevent aggregation of the Ag nanoparticles, 0.03 *g* of sodium borohydride ($Na[BH_4]$) solution was freshly prepared at a known concentration and added dropwise to each mixture. Each suspension was then subjected to ultrasonic treatment in an ultrasonic bath for 1 *h* at room temperature. After sonication, the resulting rGO/Ag/X (where X indicates the weight percentage of silver nanoparticles) nanocomposites were collected by centrifugation and subsequently dried in an oven at 40 *°C* under vacuum until a constant weight was achieved.

2.4. Preparation of rGO/Ag/PANI Nanofibers Modified Electrode

The glassy carbon electrode (GCE) was initially polished sequentially using alumina (Al_2O_3) powders of 0.3 *μm* and 0.05 *μm* particle sizes to obtain a smooth and mirror-like surface. After polishing, the electrode was thoroughly rinsed with deionized water (resistivity ≥18.2 *MΩ·cm*) and dried under a nitrogen stream to prevent contamination.

A spinning solution was prepared by dissolving 0.7 *g* of polyaniline (PANI) in chloroform under continuous stirring, followed by the addition of 0.15 *g* of camphorsulfonic acid (CSA) as a dopant to enhance the conductivity and solubility of PANI. The mixture was stirred for 24 *h* at room temperature until a homogeneous and transparent solution was obtained.

Subsequently, predetermined amounts of rGO/Ag nanocomposite (1%, 3%, 5%, and 7% *w/w* relative to PANI) were dispersed into the PANI solution. Each mixture was sonicated in an ultrasonic bath for 1 *h* to ensure uniform dispersion and prevent agglomeration of nanocomposite particles. The resultant suspensions were then electrospun onto the pre-polished GCE surface.

Electrospinning was conducted using an apparatus supplied by Fanavaran Nano-Meghyas Co. (Isfahan, Iran). The parameters were set at a voltage of 25 *kV*, a needle-to-collector distance of 20 *cm*, and a solution feed rate of 0.5 *mL/h*. Nanofibers were collected on an aluminum foil substrate attached to the collector to facilitate subsequent morphological and electrochemical characterization. The prepared electrodes were labeled as rGO/Ag/PANI/X, where X indicates the weight percentage of rGO/Ag incorporated (X = 1, 3, 5, or 7).

For functionalization, monoclonal anti-HER2 antibodies were immobilized onto the electrospun nanofiber-modified electrode surface. The antibody solution was carefully drop-cast onto the electrode and incubated at 4 *°C* for 24 *h* to promote stable antibody binding. After immobilization, the electrode was gently rinsed with phosphate-buffered saline (PBS, pH 7.4) to remove unbound antibodies and stored at 4 *°C* until use (Figure 1).

p-ISSN 0854-1418
e-ISSN 2503-426X

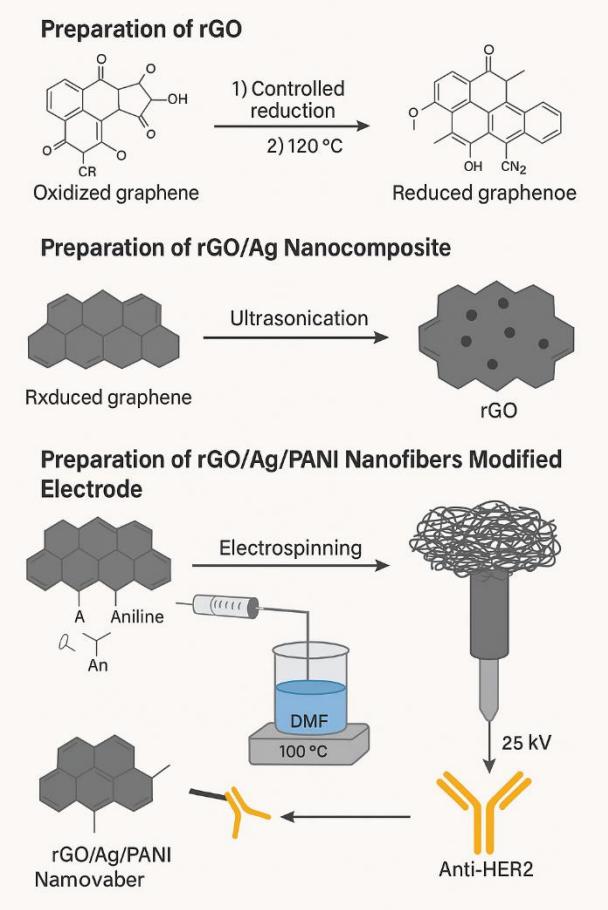

Fig 1: schematic for the preparation of samples.

2.4. Characterization

2.4.1. Chemical and Physical Characterizations

The chemical properties of the electrospun nanofiber scaffolds were characterized using Fourier-transform infrared (FTIR) spectroscopy (ThermoNicolet NEXUS 870 FTIR, Nicolet Instrument Corp., USA), allowing for the identification of functional groups and bonding interactions. The surface morphology and topography of the nanofibers were examined through Field Emission Scanning Electron Microscopy (FESEM) (Sigma, Zeiss, Germany) and Atomic Force Microscopy (AFM) (ENTEGRA MDT-AFMNT, NT-MDT Co.), respectively. The average diameter of various nanofibers was determined by an image processor (SXM-196X).

X-ray diffraction (XRD) analysis was conducted using a D/max 2500 XRD spectrometer (Rigaku), employing a Cu Kα radiation source with a wavelength of 0.1541 *nm*, to assess the crystallographic structure of the nanocomposites. The specific surface area of the nanofibers was measured via the Brunauer–Emmett–Teller (BET) method using a BElSORP Mini analyzer (Microtrac Bel Corp.), while pore size distribution was determined through the Barrett–Joyner–Halenda (BJH) model, based on nitrogen desorption isotherms, using the same instrument.

2.4.2. Electromechanical Characterization

Cyclic voltammetry (CV) measurements were performed using a high-precision potentiostat/galvanostat (Autolab PGSTAT100N, Metrohm Co.), configured in a conventional three-electrode setup. The working electrode was either a bare or modified glassy carbon electrode (GCE) with a diameter of 3 *mm*. A platinum wire was employed as the counter electrode, providing the current path, while a silver/silver chloride (Ag|AgCl) electrode, immersed in a saturated potassium chloride (KCl) solution, functioned as the reference electrode. This setup ensured stable potential control and precise electrochemical measurements.

3. RESULTS AND DISCUSSION

3.1. FTIR Analysis

Fourier-transform infrared (FTIR) spectroscopy was employed to qualitatively investigate the chemical structure and interfacial interactions among graphene oxide (GO), reduced graphene oxide (rGO), silver nanoparticles (AgNPs), and their nanocomposite forms (rGO/Ag). Figure 2 and Table 1 present the relevant absorption bands and corresponding functional groups, offering insights into the chemical transformations that occurred during the material synthesis and functionalization processes.

In the FTIR spectrum of GO, prominent absorption bands were identified at ~1,720 cm^{-1} (C=O stretching of carboxyl groups), ~1,200 cm^{-1} (C–OH stretching of hydroxyl groups), ~1,020 cm^{-1} (C–O–C stretching of epoxide or ether groups), and ~3,430 cm^{-1} (O–H stretching of hydroxyl and adsorbed water), all indicative of a highly oxygenated carbon framework [28–36]. These oxygen-containing functional groups impart GO with hydrophilicity and chemical reactivity, but also disrupt its π-conjugated structure.

Upon chemical reduction, rGO exhibited a significant attenuation or disappearance of the aforementioned oxygen-related peaks, particularly the C=O and O–H bands. This reflects the successful removal of carboxyl, hydroxyl, and epoxide groups via electron transfer reactions, likely facilitated by sodium borohydride ($NaBH_4$) as a strong reducing agent [37–40]. Concomitantly, a stronger peak emerged at ~1,600 cm^{-1}, corresponding to C=C stretching in sp^2-hybridized carbon domains, suggesting partial restoration of the graphitic conjugated π-system and improvement in electrical conductivity [41]. However, the residual presence of weak oxygen-related peaks implies incomplete reduction, which is common and may actually favor further chemical interactions within the composite matrix.

The FTIR spectrum of AgNPs revealed a weak yet distinguishable band near ~517 cm^{-1}, which is attributed to Ag–O stretching vibrations, indicating the formation of a thin layer of silver oxide on the nanoparticle surfaces due to ambient oxidation [42–45]. Other notable bands include those at ~3,436 cm^{-1} (N–H or O–H stretching), ~2,917 cm^{-1} (C–H stretching of aliphatic chains), and 1,009–1,111 cm^{-1} (C–N or C–O stretching), which are likely due to residual organic species, such as stabilizers, capping agents, or remnants of the reaction medium (e.g., DMF or surfactants) [46–52]. These surface functionalities may aid in nanoparticle stabilization and dispersion, while also providing reactive sites for interaction with the rGO matrix.

The FTIR spectra of rGO/Ag nanocomposites revealed combined features of both rGO and AgNPs, with some notable shifts and intensity variations. Bands appearing around ~1,300 cm^{-1} and ~1,650 cm^{-1} may indicate the presence of NO_2- or amine-like functionalities, potentially originating from residual nitrate ions in $AgNO_3$ precursor solutions [53,54]. These bands may result from partial coordination or surface adsorption rather than covalent bonding. Nonetheless, due to the lack of direct compositional data such as XPS or CHNS analysis, these interpretations remain tentative and should not be considered definitive [55].

In terms of interfacial interactions, it is hypothesized that AgNPs may be partially stabilized on the rGO surface via electrostatic forces or weak coordination between residual oxygen-containing groups (e.g., hydroxyl, carbonyl) and silver ions during the in-situ synthesis. The π–π stacking interactions among rGO sheets, combined with the spatial separation introduced by embedded AgNPs, likely contribute to structural stabilization and increased surface accessibility. Furthermore, the observed decrease in FTIR band intensities associated with hydroxyl and carboxyl groups upon composite formation may reflect partial consumption of these groups during AgNP immobilization or reduction.

In summary, FTIR analysis provides evidence for the successful reduction of GO to rGO and the subsequent functional integration of AgNPs. However, FTIR, being primarily qualitative, cannot determine the exact stoichiometry or oxidation state distributions. As such, the chemical interpretations derived from these spectra should be considered indicative. More definitive conclusions regarding elemental composition and oxidation states would require complementary techniques such as X-ray photoelectron spectroscopy (XPS), energy-dispersive X-ray spectroscopy (EDX), or elemental analysis.

Table 1. Representative FTIR absorption bands and assigned functional groups

Sample	Wavenumber (cm^{-1})	Assigned Functional Group	Reference
GO	~1,720	C=O (carboxylic)	[32–34]
	~1,020	C–O–C (epoxy/ether)	[28,30]
	~3,430	O–H (hydroxyl, H-bonded)	[35]
rGO	~1,600	C=C (sp^2 carbon domains)	[40,41]
	↓ in O–H, C=O	Partial deoxygenation	[37–39]
AgNPs	~517	Ag–O (silver oxide surface layer)	[42–44]
	~2,917	C–H (aliphatic)	[50,51]
	~3,436	O–H / N–H (surface adsorbates)	[46–48]
rGO/Ag	~1,300–1,650	Possibly NO_2 or N–H (tentative)	[53–55]
	~1,200	C–O (alkoxy or ether)	[56]

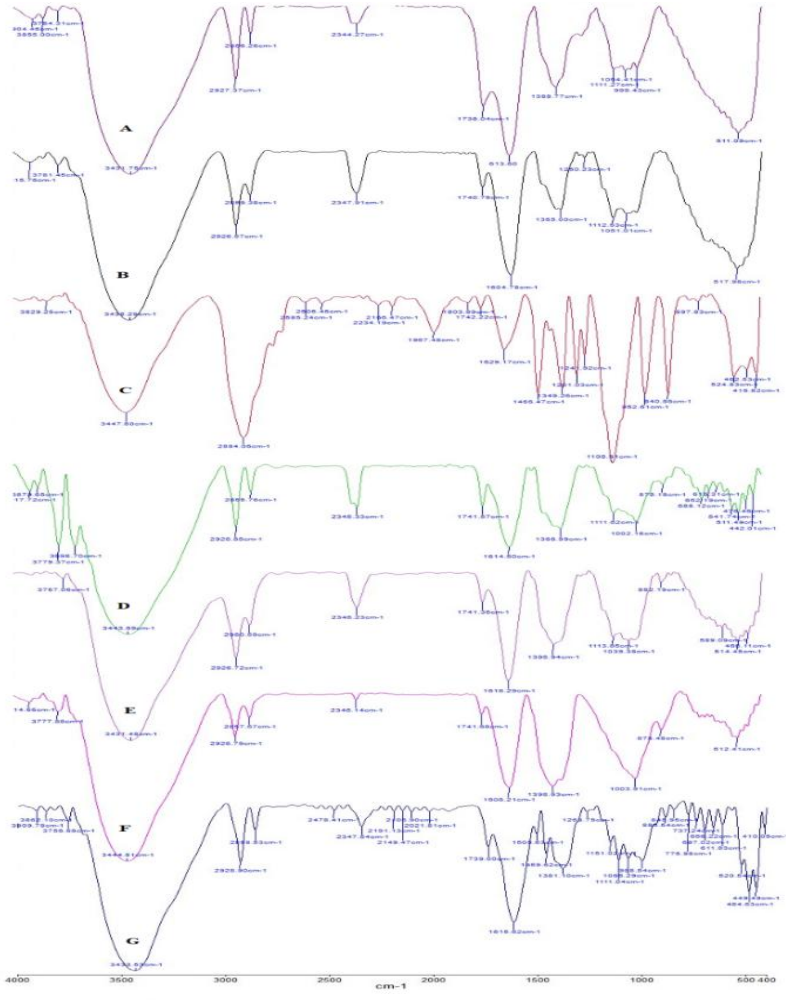

Fig 2: FTIR spectra of **A)** GO nanoparticles, **B)** rGO nanoparticles, **C)** Ag nanoparticles, **D)** rGO/Ag/1 nanocomposite, **E)** rGO/Ag/2 nanocomposite, **F)** rGO/Ag/3 nanocomposite and **G)** rGO/Ag/4 nanocomposite.

3.2. Crystallography Analysis

X-ray diffraction (XRD) was employed to investigate the crystallographic structure, phase composition, and degree of crystallinity of the synthesized materials, including GO, rGO, AgNPs, and rGO/Ag nanocomposites with varying silver contents. The corresponding diffraction patterns are presented in Figure 3A–G.

The XRD spectrum of graphene oxide (GO) (Figure 3A) exhibits a distinct and sharp peak at $2\theta \approx 10.9°$, which corresponds to the (001) diffraction plane. This reflection is indicative of the regular lamellar stacking of oxidized

graphene sheets, resulting from the intercalation of oxygenated functional groups such as hydroxyl, carboxyl, and epoxide moieties between the basal planes [58, 59]. Upon chemical reduction, the GO peak disappears and is replaced by a broad diffraction feature centered at approximately $2\theta \approx 24.1°$ in the rGO sample (Figure 3B), corresponding to the (002) plane of graphitic carbon. This shift reflects a significant decrease in interlayer spacing and ordering, attributed to the removal of oxygen functionalities and partial restoration of the sp^2-hybridized carbon network [60, 61]. The broad nature of the peak indicates an increased structural disorder and reduced crystallinity, consistent with the exfoliation and partial restacking of graphene layers after reduction.

The diffraction pattern of synthesized silver nanoparticles (AgNPs) (Figure 3C) reveals intense and well-defined peaks at $2\theta \approx 38.1°$, 44.3°, 64.4°, and 77.4°, corresponding to the (111), (200), (220), and (311) planes of face-centered cubic (FCC) metallic silver, respectively [62–64]. The absence of secondary peaks confirms the high phase purity and crystallinity of the AgNPs, with no detectable impurities or oxide phases. The calculated interplanar spacing (d-values) aligns well with standard FCC Ag, further validating the formation of pure crystalline silver.

The XRD patterns of rGO/Ag nanocomposites synthesized with various Ag loadings (Figure 3D–G) display the same characteristic peaks of FCC silver, confirming the successful incorporation of AgNPs into the rGO matrix [65–67]. The intensity of the (111) peak at ~38.1° was particularly dominant across all compositions, signifying the preferential growth orientation of AgNPs. The rGO (002) diffraction signal remains visible but attenuated, suggesting partial retention of the graphitic structure post-hybridization. This reduction in rGO peak intensity is likely due to the homogeneous dispersion of AgNPs over the rGO surface, which disrupts regular stacking and introduces additional structural disorder.

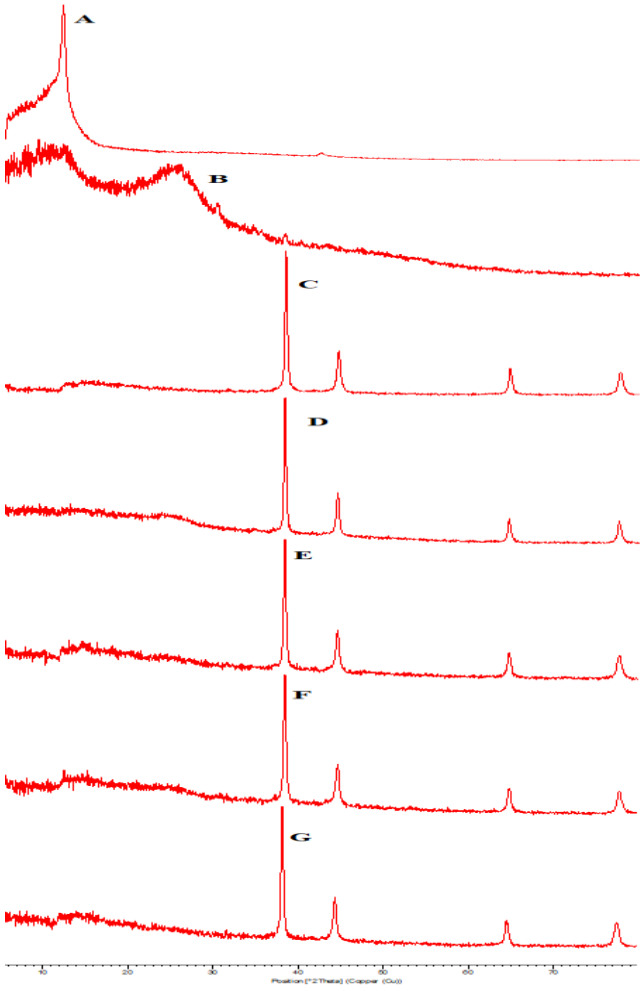

Fig 3: XRD spectra of **A)** GO nanoparticles, **B)** rGO nanoparticles, **C)** Ag nanoparticles, **D)** rGO/Ag/1 nanocomposite, **E)** rGO/Ag/2 nanocomposite, **F)** rGO/Ag/3 nanocomposite and **G)** rGO/Ag/4 nanocomposite.

To further elucidate the effect of Ag loading on crystal size, the average crystallite dimensions of AgNPs in the composites were estimated using the Debye–Scherrer equation [68]:

$$D = \frac{k\,\lambda}{\beta\ \csc\theta} \qquad (1)$$

where D is the average crystallite size (*nm*), k is the shape factor (typically 0.9), λ is the X-ray wavelength (0.154 nm for Cu Kα radiation), β is the full width at half maximum (FWHM) in radians, and θ is the Bragg angle. The analysis revealed a slight decrease in crystallite size with increasing silver content, which may be attributed to improved dispersion and nucleation control of AgNPs in the rGO framework. This enhanced dispersion likely facilitates stronger interfacial interactions between rGO and AgNPs, which could contribute to improved electrochemical properties, including higher catalytic activity and better electron transport in the final sensing platform.

Table 2. The crystallite size of the different samples under Scherer's formula

Sample	The range of crystal size (*nm*)	Average crystal size (*nm*)
GO	9.68 – 17. 50	13.50
rGo	1.98 – 49.91	19.49
AgNPs	19.01 -34.05	25.30
rGo / Ag/1	23.43 - 33.32	27.51
rGo / Ag/2	23.43 - 33.32	27.51
rGo / Ag/3	23.43 - 33.32	27.51
rGo / Ag/4	23.43 - 33.32	27.51

3.3. BET & BJH Analysis

The surface textural properties of the synthesized samples were systematically analyzed using Brunauer–Emmett–Teller (BET) and Barrett–Joyner–Halenda (BJH) methods, providing quantitative insights into their specific surface area, pore volume, and pore size distribution. These parameters are of paramount importance for optimizing material performance in electrochemical biosensing.

The BET method, based on nitrogen physisorption at 77 *K*, quantifies the monolayer adsorption capacity (V_m), from which the specific surface area (S_{BET}) is derived according to the equation:

$$S_{BET} = \frac{N \times a \times V_m}{m} \qquad (2)$$

where N is Avogadro's number, a is the effective cross-sectional area of a nitrogen molecule (0.162 nm^2), V_m is the monolayer volume of nitrogen adsorbed, and m is the sample mass [69–71].

As summarized in Table 3, the pure silver nanoparticles showed a relatively low surface area of 3.16 m^2/g, reflecting their dense, non-porous morphology and aggregation behavior [72]. In contrast, graphene oxide (GO) exhibited a high specific surface area of 9.88 m^2/g, consistent with its two-dimensional structure, abundant oxygenated functional groups, and high density of accessible adsorption sites [73]. Upon chemical reduction, the specific surface area of reduced graphene oxide (rGO) decreased to 5.09 m^2/g due to the elimination of oxygen functionalities and increased π–π stacking between graphene sheets, which leads to partial restacking and reduces surface accessibility [74,75].

p-ISSN 0854-1418
e-ISSN 2503-426X

Table 3. The specific surface area values of different samples

Samples	Surface Area (m^2/g)	Pore Diameter (nm)	Pore Volume (cm^3/g)
GO	9.8787	1.96	0.024434
rGo	5.0878	2.21	0.030723
AgNPs	3.1554	34.75	0.037259
rGo /Ag/1	4.2150	2.06	0.026000
rGo /Ag/2	3.9080	1.93	0.022000
rGo /Ag/3	3.4340	1.74	0.020000
rGo /Ag/4	4.7150	2.18	0.031000

Incorporation of Ag nanoparticles into the rGO matrix resulted in a further decrease in surface area as Ag occupied active sites and potentially promoted partial agglomeration. Among the nanocomposites, the rGO/Ag sample with 3 *wt%* Ag displayed the lowest surface area (3.43 m^2/g), indicating the most significant blocking of surface adsorption sites. Interestingly, with further Ag addition up to 4 *wt%*, the surface area increased again to 4.71 m^2/g. This behavior may be related to improved dispersion of silver nanoparticles at higher loading, generating new interfacial voids or disrupting the stacking of rGO layers, thereby restoring additional accessible surface sites [76]. The trend is well illustrated in Figure 4, which depicts the relationship between Ag content and surface area.

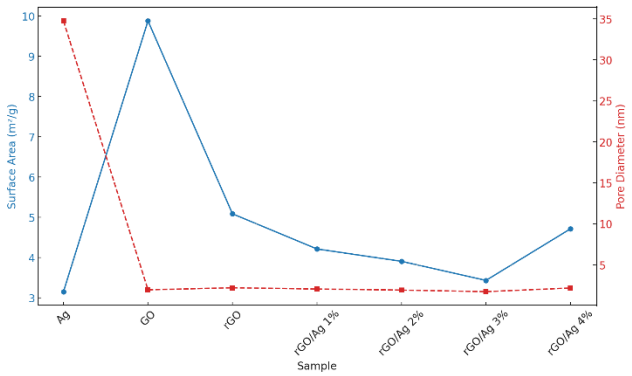

Fig 4: Surface area and pore diameter of different samples.

BJH analysis further complemented the BET data by providing the pore size distribution and pore volume. As expected, the pure Ag nanoparticles displayed the largest average pore diameter (34.75 *nm*) and the highest pore volume (0.0373 cm^3/g), which is attributable to interparticle voids rather than inherent porosity [77]. Graphene oxide, on the other hand, exhibited a much smaller average pore size of 1.96 *nm* and pore volume of 0.0244 cm^3/g, characteristic of its interlayer spacing and defect-rich structure [78,79]. After reduction to rGO, the average pore diameter slightly increased to 2.21 *nm* with a pore volume of 0.0307 cm^3/g, likely due to nanosheet restacking and agglomeration, collapsing smaller micropores but introducing mesoporous gaps [80].

The addition of Ag nanoparticles to rGO progressively reduced pore size and volume up to a loading of 3 *wt%*, suggesting partial pore blockage and increased packing density. However, similar to the surface area trend, at 4 *wt%* Ag, both pore diameter (2.18 *nm*) and pore volume (0.031 cm^3/g) increased again, possibly due to re-dispersion of the silver nanoparticles, which interrupts dense stacking and introduces mesoporous regions. This pattern supports the conclusion that Ag content strongly influences the textural parameters of the rGO-based nanofibers.

Collectively, these BET and BJH results demonstrate that the specific surface area and porosity of the synthesized materials can be precisely tuned by controlling the silver nanoparticle loading. Such tunability is crucial for

p-ISSN 0854-1418
e-ISSN 2503-426X

maximizing the electrochemical active surface and optimizing the sensitivity and stability of the biosensing platform.

3.4. FESEM Analysis

Field emission scanning electron microscopy (FE-SEM) was utilized to systematically examine the surface morphology and structural evolution of graphene oxide (GO), reduced graphene oxide (rGO), and a series of rGO/Ag nanocomposites containing varying silver nanoparticle concentrations. The micrographs (Figure 5A–F) offer valuable insights into how silver incorporation affects the morphological attributes of the graphene-based matrix, which in turn influences the composite's functional performance, particularly for biosensing applications.

The FE-SEM image of GO (Figure 5A) reveals a typical multilayered lamellar structure with crumpled, loosely stacked nanosheets that form a porous and sponge-like texture. This morphology is consistent with a high density of oxygenated functional groups—such as hydroxyl, epoxide, and carboxyl—distributed over both basal planes and sheet edges [81, 82]. These polar functionalities induce capillary hydration effects, yielding a soft, carpet-like texture with interconnected nanochannels and high surface area [83-85].

Upon chemical reduction (Figure 5B), the GO undergoes a morphological transformation into rGO, exhibiting fewer layers and a more compact, wavy, and wrinkled morphology with a silk-like appearance [85, 86]. This is attributed to the partial elimination of surface oxygen groups and the reestablishment of π–π stacking interactions between graphene sheets, enhancing electrical conductivity and surface accessibility [84, 86].

Figures 5C–E display the FE-SEM micrographs of rGO/Ag/1, rGO/Ag/2, and rGO/Ag/3 nanocomposites, respectively. Silver nanoparticles appear as uniformly dispersed, spherical features anchored onto the rGO surfaces, acting as interlayer spacers that prevent re-stacking of graphene sheets. This distribution is critical in maintaining a high degree of sheet exfoliation, thus ensuring access to active sites and enabling effective charge transport throughout the nanocomposite [85]. Importantly, among all investigated compositions, the rGO/Ag/3 sample (Figure 5E) demonstrates the most optimal morphology. It strikes an ideal balance between Ag nanoparticle density and sheet separation, ensuring uniform dispersion without agglomeration, while retaining the desirable wrinkled architecture of rGO. This synergistic microstructure maximizes electroactive surface area and enhances electron transfer kinetics, essential for biosensing sensitivity and stability.

In contrast, the rGO/Ag/4 nanocomposite (Figure 5F) shows increased Ag nanoparticle loading (≈58–172 *nm*) with denser surface coverage. While the particles remain largely discrete, partial aggregation is evident, which may lead to local conductivity disruptions or hinder mass transport. Although the wrinkled morphology persists, the excessive nanoparticle density could partially obscure the active surface and reduce effective analyte accessibility [85].

Taken together, the FE-SEM analysis indicates that rGO/Ag/3 offers the most favorable microstructural configuration for subsequent integration into polyaniline (PANI) nanofiber networks and electrode modification. The optimized distribution of Ag nanoparticles, combined with preserved nanosheet undulation and interlayer spacing, positions this composite as the most suitable platform for achieving high-performance biosensing. This morphology is anticipated to provide enhanced signal amplification, reduced response time, and reliable detection of HER2-positive cells in complex biological media.

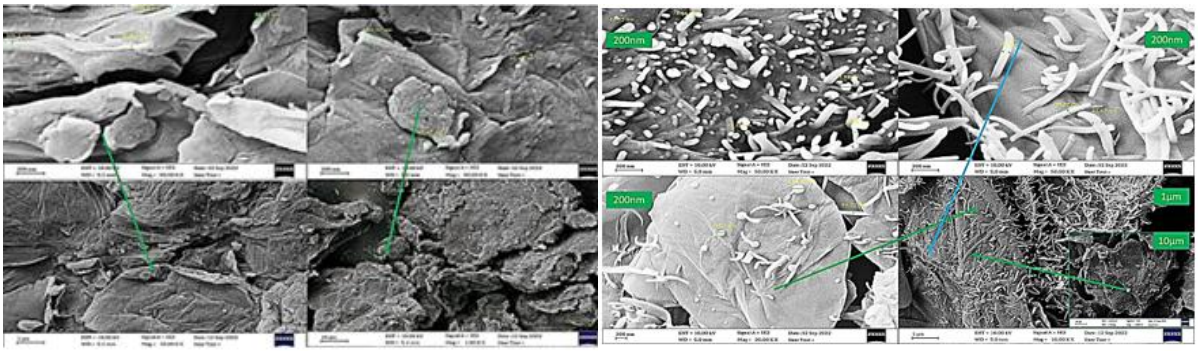

p-ISSN 0854-1418
e-ISSN 2503-426X

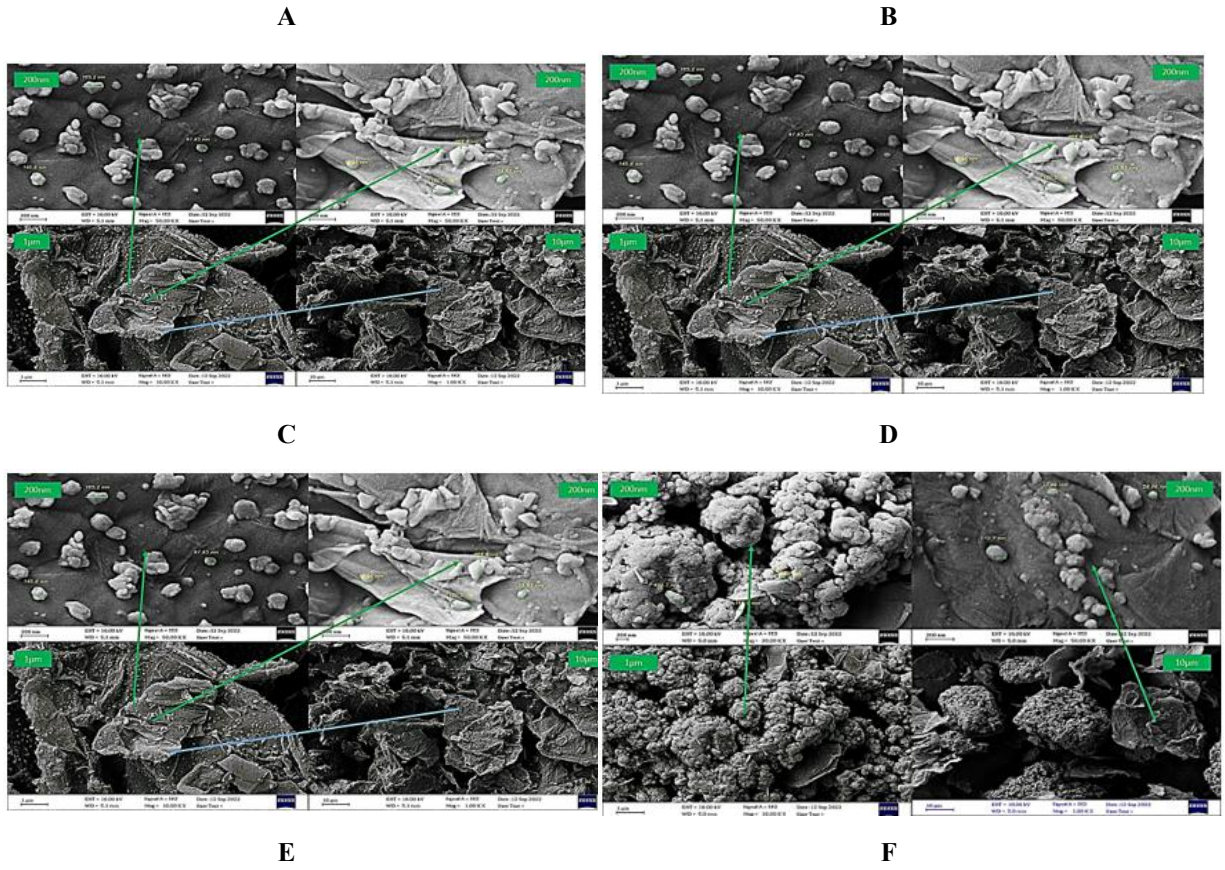

Fig 5. FESEM images of samples **A)** GO nanoparticles, **B)** rGO nanoparticles, **C)** Ag nanoparticles, **D)** rGO/Ag/1 nanocomposite, **E)** rGO/Ag/2 nanocomposite, **F)** rGO/Ag/3 nanocomposite and **G)** rGO/Ag/4 nanocomposite.

Field emission scanning electron microscopy (FE-SEM) was employed to investigate the morphological characteristics of pristine polyaniline (PANI) nanofibers and those reinforced with varying concentrations of the optimized rGO/Ag nanocomposite. The resulting micrographs, depicted in Figure 6A–I, offer a detailed assessment of how nanocomposite incorporation influences fiber morphology, continuity, and distribution uniformity—factors crucial to the electrical and mechanical performance of electrospun structures.

As illustrated in Figure 6A, the pure PANI nanofibers exhibit a uniform and continuous cylindrical morphology with smooth surfaces and well-defined diameters. This structural uniformity is indicative of favorable electrospinning conditions and polymer chain alignment, which are essential for maintaining the electroactive and conductive behavior of PANI [87].

Incorporation of rGO/Ag nanocomposite into the PANI matrix (Figures 6B–F) initially preserves the morphological integrity of the nanofibers. At lower concentrations (1–4 *wt%*), the rGO/Ag nanoparticles are well-dispersed within the PANI solution, resulting in homogeneously distributed nanofibers without apparent phase separation or aggregation. The absence of bead-like defects or irregularities in this range reflects the effective stabilization of the hybrid solution, likely due to the uniform anchoring of rGO and Ag nanoparticles on the PANI chains [88]. This consistent morphology contributes positively to the mechanical strength and electron transport pathways within the nanofibers.

However, as the rGO/Ag content increases to 5 *wt%* and beyond (Figures 6G–H), significant morphological changes become evident. The fibers begin to exhibit surface roughness, irregularities, and localized adhesion at the intersection points—phenomena typically associated with nanoparticle agglomeration and polymer chain crosslinking [89]. These effects can be attributed to an increase in solution viscosity arising from enhanced

p-ISSN 0854-1418
e-ISSN 2503-426X

intermolecular interactions and nanoparticle crowding. Elevated viscosity compromises fiber uniformity during electrospinning, resulting in distorted fiber geometry and fusion at junctions [90,91]. Such changes may negatively impact fiber porosity and flexibility, and thus must be carefully controlled in the optimization of nanofiber-based devices.

To further elucidate the internal nanostructure, transmission electron microscopy (TEM) analysis was conducted on the rGO/Ag/PANI nanofibers containing 4 *wt%* nanocomposite (Figure 6I). The TEM image clearly reveals the presence of rGO/Ag nanodomains as dark contrast regions distributed along the fiber surface and within the fiber walls. These observations confirm the successful integration of both reduced graphene oxide and silver nanoparticles into the PANI matrix. The homogeneous distribution and intimate contact between the nanocomposite and the polymer backbone are expected to facilitate enhanced electrochemical activity by promoting efficient charge transfer and increasing the density of reactive surface sites [92].

Collectively, the FE-SEM and TEM analyses demonstrate that the rGO/Ag/PANI/3 and /4 compositions maintain an optimal balance between fiber integrity and nanocomposite dispersion. Among them, the rGO/Ag/PANI/3 formulation appears to offer the most favorable morphology for sensor fabrication, minimizing agglomeration while maximizing electrochemical surface area. [92].

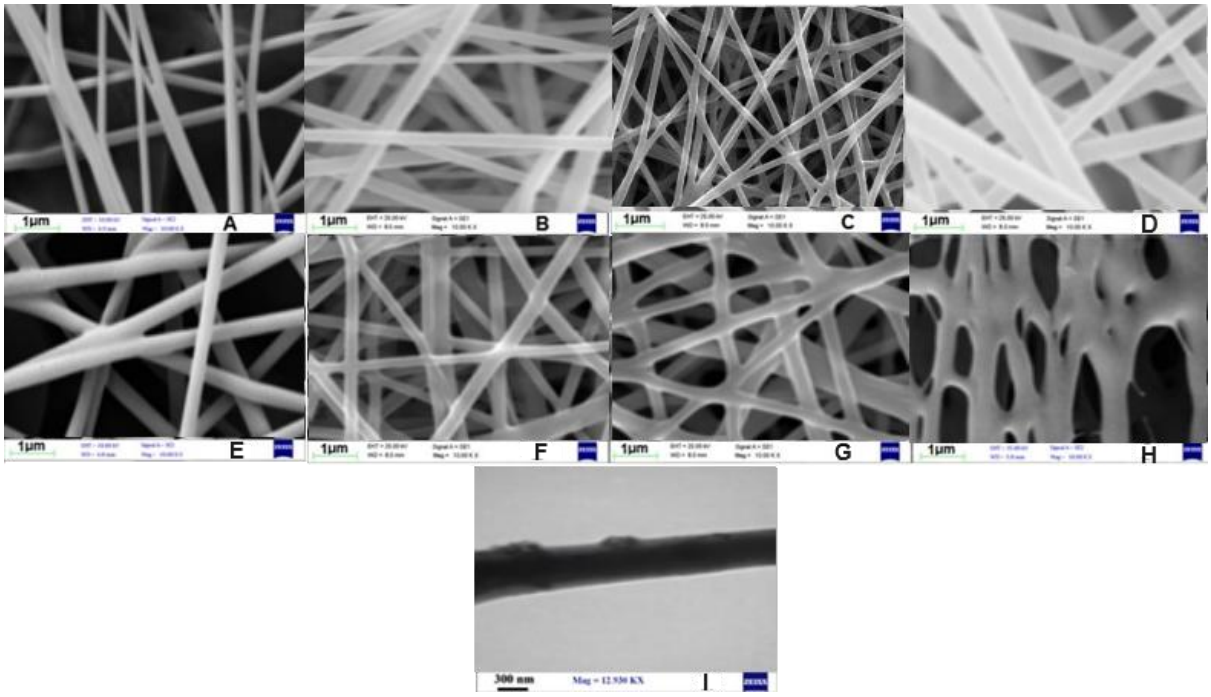

Fig 6. FESEM images of nanofibers of **A)** PANI **B)** rGO/Ag/PANI/1, **C)** rGO/Ag/PANI/2, **D)** rGO/Ag/PANI/3, **E)** rGO/Ag/PANI/4, **F)** rGO/Ag/PANI/5, **G)** rGO/Ag/PANI/6, **H)** rGO/Ag/PANI/7 and I) TEM image of rGO/Ag/PANI/5.

The influence of rGO/Ag nanocomposite incorporation on the diameter distribution of electrospun nanofibers was systematically examined, and the results are presented in Figure 7. The quantitative analysis reveals a clear, progressive increase in average fiber diameter with increasing rGO/Ag content in the PANI polymer matrix. The mean diameters measured for PANI, rGO/Ag/PANI/1, rGO/Ag/PANI/2, rGO/Ag/PANI/3, rGO/Ag/PANI/4, rGO/Ag/PANI/5, rGO/Ag/PANI/6, and rGO/Ag/PANI/7 were approximately 105.11, 121.37, 132.11, 159.59, 188.45, 261.97, 326.38, and 386.49 *nm*, respectively.

This observed diameter escalation is strongly correlated with the increasing concentration of rGO/Ag nanofillers, which significantly alter the rheological behavior of the electrospinning solution. Specifically, the presence of conductive nanomaterials—particularly reduced graphene oxide and silver nanoparticles—promotes interfacial

p-ISSN 0854-1418
e-ISSN 2503-426X

interactions and potential crosslinking with the polyaniline backbone. These interactions contribute to a rise in solution viscosity, resulting in thicker jet streams during electrospinning and consequently larger fiber diameters.

Such a trend is consistent with previously reported findings, where the integration of nanofillers into polymer matrices has been shown to increase fiber thickness due to enhanced chain entanglement, increased charge density, and modification of electrohydrodynamic forces during jet elongation [93–95]. Furthermore, the size increment may be indicative of nanoparticle-induced morphological stabilization, which can positively influence the mechanical robustness and surface functionality of the resulting fibers.

Importantly, while moderate increases in fiber diameter may be beneficial in terms of mechanical strength and nanocomposite dispersion, excessive nanoparticle loading—as observed in rGO/Ag/PANI/6 and /7—could result in inhomogeneities and agglomeration, potentially compromising fiber uniformity and surface area. Therefore, these results emphasize the critical need to optimize rGO/Ag concentration to balance structural integrity, electrochemical performance, and morphological consistency in electrospun nanofiber systems.

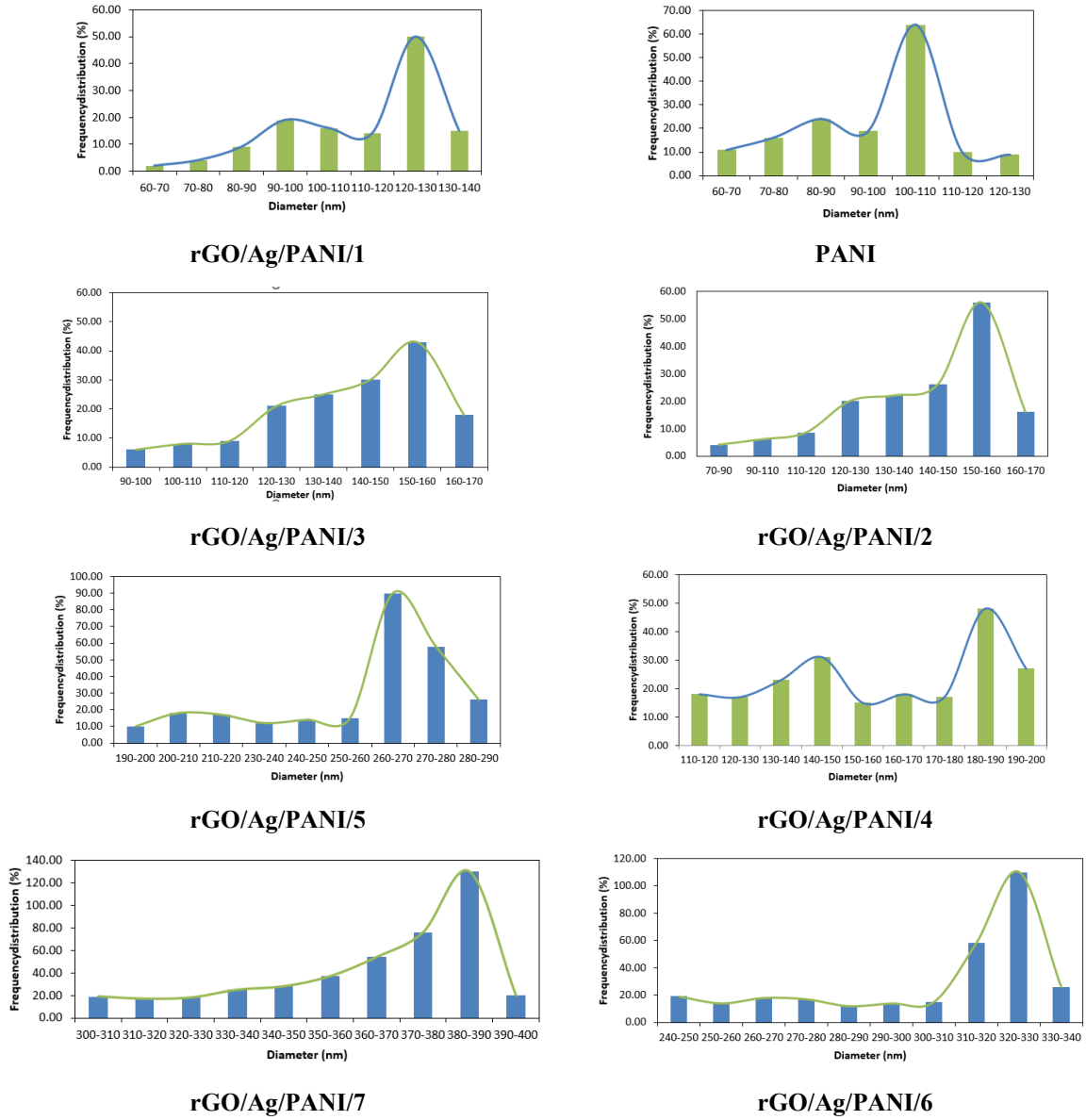

Fig 7. Nanofiber diameter size distribution diagram for different samples.

Atomic force microscopy (AFM) was employed to evaluate the surface morphology and nanoscale roughness of electrospun nanofibers, offering complementary insights into nanoparticle distribution and surface texture. Representative AFM images of pure polyaniline (PANI) and rGO/Ag/PANI/4 nanofibers are shown in Figure 8. The arithmetic mean surface roughness (S_a), calculated from the topographical profiles, was determined to be 20.2 *nm* for pristine PANI nanofibers and increased to 29.7 *nm* for the rGO/Ag/PANI/4 nanocomposite.

This marked increase in surface roughness upon incorporation of the rGO/Ag nanocomposite suggests successful integration and uniform dispersion of nanoparticles within the polymer matrix. The enhanced roughness can be attributed to the surface protrusions formed by rGO nanosheets and silver nanoparticles, which are known to partially embed within and decorate the nanofiber surface. Such nanoscale heterogeneity is consistent with previous reports, where the presence of folded and crumpled graphene sheets within nanocomposites significantly contributed to increased surface irregularity and accessible interfacial area [96–99].

Topographical features observed in the rGO/Ag/PANI/4 sample further indicate a roughened, granular morphology with elevated surface energy, which is advantageous for applications requiring high analyte adsorption, such as electrochemical biosensing and catalysis. The observed increase in roughness may also enhance electrical conductivity by increasing the density of charge transfer pathways across the fiber surface.

Overall, AFM analysis confirms the morphological transformation induced by rGO/Ag incorporation and underscores its positive impact on both the physicochemical and functional properties of the nanofibers. These surface modifications are expected to play a pivotal role in optimizing sensor response, interaction kinetics, and mechanical robustness in advanced functional nanomaterials.

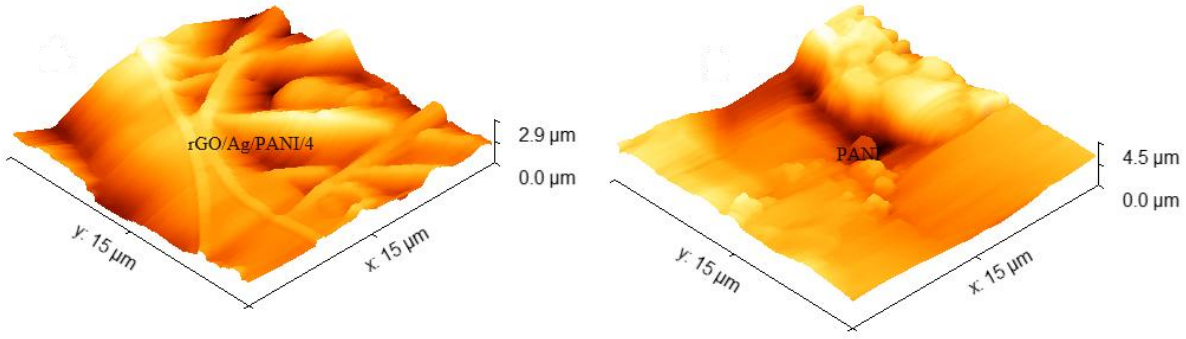

Fig 8. AFM images of different modified electrodes

3.5. Electrochemical Characterization of the Modified Electrode

Electrochemical impedance spectroscopy (EIS), represented by Nyquist plots (Figure 9a–d), was employed to evaluate the interfacial electron transfer behavior of the sensor at different fabrication stages: bare glassy carbon electrode (GCE), rGO/Ag/PANI-modified GCE, BSA-blocked surface (rGO/Ag/PANI/GCE/BSA), and after immobilization of SK-BR3 breast cancer cells (rGO/Ag/PANI/GCE/BSA/SK-BR3). This technique provides detailed insights into the electrode/electrolyte interface and the dynamics of charge transfer resistance (R_{ct}), a key parameter for biosensing performance.

As shown in the EIS spectra, the bare GCE exhibited a relatively high R_{ct} value, indicative of sluggish electron transfer kinetics at the unmodified electrode surface. Upon modification with the rGO/Ag/PANI nanostructure, a substantial decrease in the semicircular diameter of the Nyquist plot was observed, reflecting a significant reduction in R_{ct}. This enhancement in interfacial conductivity is attributed to the synergistic effects of the nanocomposite constituents: reduced graphene oxide (rGO) with its high charge mobility and surface area, silver nanoparticles (AgNPs) offering excellent catalytic properties and electron pathways, and polyaniline (PANI) contributing a highly conductive, redox-active polymer network [100].

Following the covalent immobilization of anti-HER2 monoclonal antibodies onto the nanocomposite-modified GCE, a notable increase in R_ct was recorded. This behavior is consistent with the formation of a bio-insulating layer, as antibodies are non-conductive biomacromolecules that hinder electron transfer by physically blocking active sites on the electrode surface [101]. The rise in impedance at this stage serves as evidence of successful biorecognition element immobilization.

Subsequent incubation of the antibody-functionalized electrode with HER2-overexpressing SK-BR3 breast cancer cells led to a further pronounced increase in R_{ct}. This effect stems from the specific antigen–antibody binding events occurring on the sensor interface, where the captured cancer cells—also non-conductive—form a dense layer that significantly impedes charge transfer. The observed impedance augmentation confirms the selective recognition and immobilization of target cells, demonstrating the sensor's diagnostic specificity [102,103].

In summary, the stepwise evolution of R_{ct} throughout the electrode modification process substantiates the successful construction of a highly sensitive and selective biosensor. The distinct impedance signatures at each stage not only validate the functionalization strategy but also affirm the potential of this platform for label-free detection of HER2-positive breast cancer cells via specific biorecognition interactions.

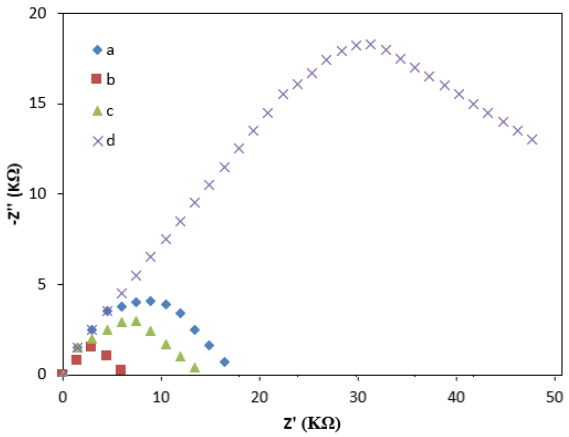

Fig 9. Nyquist plots of a) GCE, b) rGO/Ag/PANI/GCE, c) GO/Ag/PANI/GCE/BSA, and d) rGO/Ag/PANI/GCE/BSA/ SK-BR3 breast cancer cells for characterizing the surface alteration of electrode after subsequent modification in 2.5 *mM* $K_3Fe(CN)_6$ + 2.5 *mM* $K_4Fe(CN)_6$ and 0.02 *M* PBS.

3.6. Signal Optimization and Biosensing Performance Parameters

The modulation of electric current (Δj) during the bovine serum albumin (BSA) blocking step was evaluated across three electrode configurations: bare glassy carbon electrode (GCE), PANI-modified GCE (PANI/GCE), and the nanocomposite-functionalized rGO/Ag/PANI/GCE (Figure 10A). Among these, the rGO/Ag/PANI-modified electrode exhibited the highest Δj, underscoring the synergistic enhancement resulting from the incorporation of reduced graphene oxide, silver nanoparticles, and polyaniline. This composite architecture effectively increased the electron transfer rate and the electrochemically active surface area, thereby significantly improving the electrode's sensitivity for biomolecular detection applications [102,104].

To achieve maximum analytical performance, critical operational parameters—including antibody concentration, incubation time, and pH—were systematically optimized.

3.6.1. Optimization of anti-HER2 Concentration

The modified electrodes were incubated with anti-HER2 monoclonal antibodies at various concentrations (10–300 *μg/mL*), followed by exposure to 5 × 10^4 SK-BR3 *cells/mL*. As illustrated in Figure 10B, Δj increased proportionally with antibody concentration, plateauing at 200 *μg/mL*. This saturation behavior suggests that at higher concentrations, the available surface carboxylic sites on the electrode were fully occupied, limiting further antibody immobilization. Hence, 200 *μg/mL* was identified as the optimal concentration for effective antibody functionalization without inducing steric hindrance or signal suppression [105].

p-ISSN 0854-1418
e-ISSN 2503-426X

3.6.2. Optimization of Incubation Time

To ensure maximal bio-recognition efficiency, the incubation duration of the functionalized sensor with SK-BR3 cells was varied (5 to 180 *min*) under constant cell concentration. Δj increased markedly up to 30 *min*, after which the signal plateaued (Figure 10C), indicating that equilibrium binding had been reached and all available antibody sites were occupied. Thus, 30 *min* was established as the optimal incubation period, balancing binding efficiency and assay throughput.

3.6.3. Optimization of pH Conditions

Since protein structure and electrochemical interactions are highly pH-dependent, the influence of pH on biosensor performance was assessed over a range of physiologically relevant values. As shown in Figure 10D, strongly acidic conditions (pH < 6) resulted in negative Δj values, likely due to conformational denaturation of both the antibody and cell surface proteins, leading to diminished bio-affinity and non-specific interactions. A maximal and stable Δj was observed at pH 7.4, confirming that neutral physiological conditions best preserve the structural integrity and functional activity of the biomolecular recognition elements [106]. No appreciable improvement was observed at higher pH levels.

These findings collectively establish optimal biosensing conditions—namely, an anti-HER2 concentration of 200 *μg/mL*, an incubation time of 30 *min*, and a working pH of 7.4—as essential parameters for achieving high sensitivity, reproducibility, and selectivity in HER2-positive breast cancer cell detection.

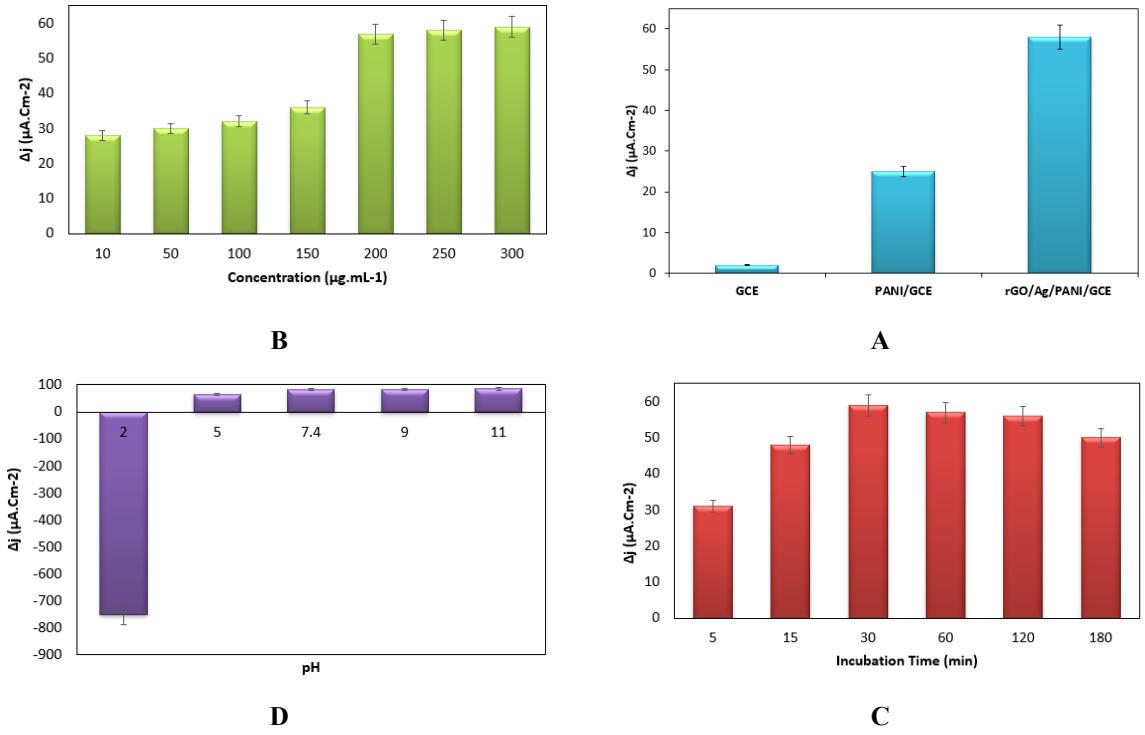

Fig 10. Optimization of the sensor performance (A) The effect of different coating over the GCE electrode on sensitivity of cancer cell detection, (B) The effect of anti-HER2 concentration on the sensitivity of cancer cell detection, (C) The effect of incubation time, and (D) The effect of pH solution on efficiency of the biosensor. The tests were done in a solution containing 2.5 *mM* $3Fe(CN)_6$ + 2.5 *mM* $K_4Fe(CN)_6$ and 0.02 *M* PBS (Every measurement was repeated three times by three different probes).

3.7. Dynamic Detection Range, Detection Limit and Selectivity of the Nanobiosensor

The optimized electrochemical cell and electrode configuration were utilized to evaluate the dynamic detection range of the biosensor for HER2-positive SK-BR3 breast cancer cells in a solution containing $Fe(CN)_6^{3-/4-}$ and phosphate-buffered saline (PBS). The differential pulse voltammetry (DPV) responses recorded at varying cell

concentrations are illustrated in Figure 11A. The resulting calibration curve exhibited excellent linearity over the tested range, with a correlation coefficient (R^2) of 0.9954 (n = 3) and a relative standard deviation (RSD) below 5%, demonstrating outstanding reproducibility and precision. The biosensor's dynamic detection range spanned from 5×10^1 to 1×10^{10} cells/mL, outperforming previously reported labeled and label-free cancer cell sensors in terms of both range and sensitivity [107]. This extensive detection window underscores the sensor's capability for accurate quantification across several orders of magnitude, enabling detection of both low and high cell concentrations.

Moreover, applying the signal-to-noise ratio (S/N = 3) criterion, the biosensor achieved an exceptional limit of detection (LOD) of 2 *cells/mL* (Figure 11B), indicative of ultra-high sensitivity. This LOD surpasses that of the majority of existing platforms for cancer cell detection, positioning the developed nanobiosensor as a highly promising tool for early-stage cancer diagnosis and clinical monitoring of minimal residual disease [108].

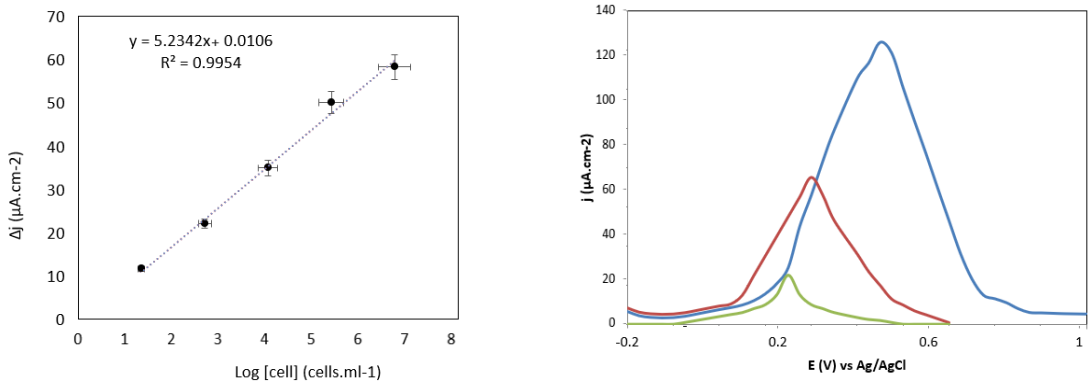

Fig 11. Detection of cancer cells. (A) Differential pulse (DP) voltammograms at 100 $mV\,s^{-1}$ scan rate for anti-HER2, BSA and different concentrations of breast cancer cells, and (B) calibration curve for different concentrations of SK-BR3 breast cancer cells under optimal sensing conditions. These tests were performed in a solution containing 2.5 *mM* $K_3Fe(CN)_6$ + 2.5 *mM* $K_4Fe(CN)_6$ and 0.02 *M* PBS (Every measurement was repeated three times by three different probes).

To evaluate the long-term stability of the biosensor, the functionalized working electrode was stored at 4 °*C* and its performance in detecting SK-BR3 breast cancer cells was assessed at 20, 40, and 60-day intervals. The biosensor retained approximately 99.9% of its initial detection efficiency throughout this period, demonstrating exceptional stability and robustness under prolonged storage conditions. Notably, the sensor maintained consistent sensitivity and accuracy in cancer cell detection over the entire 60-day timeframe, underscoring its suitability for long-term applications in cancer diagnostics. This remarkable stability highlights the durability of the nanocomposite-based electrode and confirms its potential for reliable, repeatable biosensing in clinical and research settings without significant performance degradation [109].

The biosensor also exhibited high specificity toward HER2-positive SK-BR3 cells, attributable to the strong immunoreactivity between HER2 antibodies and target cancer cells, which minimized interference from other HER2-expressing cell lines. To further validate specificity and practical utility, the sensor's performance was tested in untreated whole blood samples spiked with varying concentrations of SK-BR3 cells (5×10^2, 5×10^3, and 5×10^4 *cells/mL*), with heparin employed as an anticoagulant. Recovery experiments revealed high accuracy, with recovery efficiencies of 91.1%, 98.9%, and 96.1% respectively, relative to measurements performed in standard culture medium (Figure 12A). These results attest to the biosensor's robustness and precision in complex biological matrices, which is critical for clinical translation.

Importantly, no statistically significant difference was observed between detection performances in whole blood and culture medium (Figure 12B), further confirming the biosensor's capacity to operate effectively in physiologically relevant environments [110]. Collectively, these findings demonstrate the nano-biosensor's high functional capability and underscore its promise for clinical application in direct detection of breast cancer cells

p-ISSN 0854-1418
e-ISSN 2503-426X

from patient blood samples. The combination of exceptional stability, high specificity, and accurate recovery suggests significant potential for commercialization as a sensitive diagnostic tool for early cancer detection.

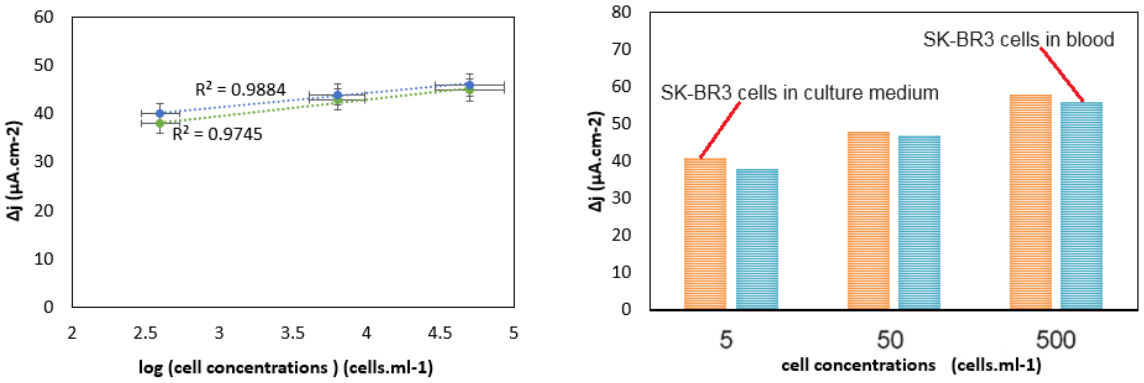

Fig 12. Nano-biosensing of cancer cells expressing different levels of HER2 (A) Recoveries and (B) Calibration curves obtained for the detection of SK-BR3 breast cancer cells in the blood samples and culture medium (The concentrations of cancer cells were set to be 5×10^2, 5×10^3 and 5×10^4 *cells* mL^{-1}).

3.8. Comparison with Literature

In addition to conventional electrochemical immunosensors, several device-centric HER2 detection strategies have been reported during 2024–2025, including transistor-based, plasmonic, SAW, and optical biosensors [111–118]. While these new platforms demonstrate excellent analytical sensitivity, most focus exclusively on HER2-ECD detection in simplified matrices and often require labeling or sample pretreatment. The present rGO/Ag/PANI nanofiber biosensor differs fundamentally by enabling direct, label-free detection of intact HER2-positive cells in complex biological samples such as whole blood, thus bridging the gap between prototype device development and real clinical applicability.

The distinctive contribution of the present device lies in its materials engineering and transduction strategy. Most contemporary HER2 biosensors rely on FET structures, plasmonic resonators, SAW resonators, or nanoparticle-labeled immunoassays, which often require complex nanofabrication, high-cost substrates, or sample preprocessing. In contrast, our rGO/Ag/PANI nanofiber-modified GCE uses a simple, scalable electrospinning process, achieves label-free impedance detection of intact HER2-overexpressing cells directly in whole blood, and demonstrates excellent stability and ultra-low LOD. Table 6 provides a device-centric comparison with relevant platforms reported between 2022–2025.

Over the past decade, electrochemical biosensors have garnered significant attention for the detection of HER2, primarily due to their high sensitivity, rapid response, and potential for miniaturized, point-of-care (POC) applications. The majority of reported platforms have focused on detecting the soluble extracellular domain of HER2 (HER2-ECD) using antibodies, aptamers, or nanomaterial-based recognition systems. While such sensors have shown favorable analytical performance under controlled conditions, their clinical translation remains limited by several persistent challenges, including the requirement for chemical labeling, surface modification complexity, lack of compatibility with unprocessed clinical samples, and an inability to detect whole HER2-overexpressing cancer cells.

For example, Freitas et al. (2021) developed a quantum dot (QD)-labeled immunosensor for HER2-ECD detection in serum with nanomolar sensitivity [2]. Despite its performance, the sensor requires multistep labeling protocols, which complicate implementation in real-time diagnostics. Similarly, Zhang et al. (2020) reported an aptasensor employing gold@MoS_2 nanohybrids, achieving a low detection limit of 0.05 *ng/mL* in buffer systems [21], but lacking validation in biologically complex media. Other reports, such as Chen et al. (2019), utilized field-effect transistor (FET)-based aptasensors offering picogram-level detection [23], although device fabrication remains cost-intensive and sample compatibility with blood or cell suspensions is limited.

Furthermore, most electrochemical HER2 biosensors target soluble biomarkers rather than whole HER2-positive cancer cells, thereby overlooking the diagnostic potential of circulating tumor cells (CTCs)—a critical indicator for metastasis and therapeutic monitoring. Additionally, many of these platforms require sample dilution, centrifugation, or chemical treatment to reduce matrix effects, hindering their utility in direct clinical testing.

In contrast, the biosensor presented in this work introduces a novel, label-free, and nanostructured sensing platform capable of detecting intact HER2-positive breast cancer cells directly in untreated whole blood. The sensor is based on a hierarchically engineered glassy carbon electrode (GCE) modified with a composite of reduced graphene oxide (rGO), silver nanoparticles (AgNPs), and polyaniline (PANI) nanofibers. Each component plays a synergistic role:

- rGO offers a high surface area and abundant functional groups for covalent antibody immobilization,
- AgNPs enhance catalytic activity and facilitate electron transfer,
- PANI provides a conductive, stable, and biocompatible matrix that supports efficient signal propagation.

This unique configuration yields a sensor with a limit of detection as low as 2 *cells/mL*, a wide dynamic range, and >90% recovery in complex whole blood samples—without any preprocessing, centrifugation, or chemical treatment. Moreover, the sensor maintains high selectivity and long-term operational stability, making it a strong candidate for real-world point-of-care diagnostics.

Table 4. Comparative Summary of Electrochemical HER2 Biosensors

Key Limitations	Pre-treatment Needed	LOD	Label-Free	Sample Matrix	Target Analyte	Sensor Type/ Modifier	Study (Year)
Requires multiple labeling steps; no whole-cell detection	*	0.1 *ng/mL*	×	Human serum	HER2-ECD (protein)	QD-labeled immunosensor	[2]
No real sample validation; low clinical relevance	×	0.05 *ng/mL*	*	Buffer	HER2-ECD (protein)	Aptasensor/ Au@MoS_2	[21]
High fabrication cost; not validated in complex matrices	×	~1 *pg/mL*	*	Buffer	HER2-ECD (protein)	FET-based aptasensor	[23]
Protein-only; requires labeled antibodies and pre-treated samples	*	0.5 *ng/mL*	×	Diluted serum	HER2-ECD (protein)	Impedimetric immunosensor	[20]
– (Direct detection of intact $HER2^+$ cells in untreated clinical sample)	×	2 *cells/mL*	*	Blood samples and culture medium	HER^{2+} cancer cells (intact)	rGO/Ag/PANI-modified GCE	This work

* yes

× No

p-ISSN 0854-1418
e-ISSN 2503-426X

For clarity, Table 5 summarizes key performance metrics of recently reported HER2 biosensors (2024–2025), including electrochemical, FET, plasmonic, SAW, and PCB-integrated platforms, allowing direct comparison with the proposed rGO/Ag/PANI sensor.

Table 5. Recent (2024–2025) device-centric HER2 biosensing platforms and their performance metrics.

Sensor Type	Target Analyte	Matrix	Label-Free	LOD	Reference
Electrochemical aptasensor (3D nanohybrid)	HER2-ECD	Serum	×	0.05 *ng/mL*	[113]
FET biosensor (graphene-based)	HER2-ECD	Buffer	*	1 *pg/mL*	[114]
SPR (plasmonic, 2D hybrid)	HER2-ECD	Serum	*	0.02 *ng/mL*	[115]
SAW biosensor	HER2-ECD	Serum	*	0.1 *ng/mL*	[116]
PCB-integrated dual-marker sensor	HER2 & CA15-3	Saliva	*	0.5 *ng/mL*	[117]
This work (rGO/Ag/PANI electrochemical)	Intact $HER2^+$ cells	Whole blood	*	2 *cells* mL^{-1}	-

* yes

× No

As summarized in Table 6, the present platform offers a unique combination of low fabrication cost, excellent stability, whole-blood compatibility, and potential for point-of-care deployment.

Table 6. Device-level comparison of recent HER2 biosensing platforms and the present work.

Sensor Type	Device Innovation	Transduction Mechanism	Target	Sample Matrix	LOD	Stability / Regeneration	Fabrication Complexity	Miniaturization Potential	Cost Category	Reference
FET (Graphene-based)	High-mobility nano-FET structure	Conductance change	HER2-ECD	Buffer / Serum	~1 pg/mL	Moderate	High (lithography, cleanroom)	High	$$$	[119]
Plasmonic SPR (2D hybrid)	Plasmonic resonance enhanced by 2D materials	SPR shift	HER2-ECD	Serum	0.02–0.1 ng/mL	Limited	Medium–High (Au coating, microfabrication)	Medium	$$–$$$	[120]

p-ISSN 0854-1418
e-ISSN 2503-426X

SAW biosensor	Acoustic mass-loading resonator	Frequency shift	HER2-ECD	Serum	0.1–1 ng/mL	Good	Mmedium (piezoelectric substrates)	High	$$	[121]
Electrochemical aptasensor	3D nanohybrid aptamer interface	DPV	HER2-ECD	Serum	0.05 ng/mL	Poor–Moderate	Medium	Medium	$$	[122]
PCB-integrated impedance	Low-cost printed microelectrodes	Impedance	HER2	Saliva	0.5 ng/mL	Good	Low (printed circuit board)	Very High	$	[123]
This work (rGO/Ag/PANI)	Hybrid nanofiber network; direct whole-cell detection	Impedance (EIS)	$HER2^{+}$ intact cells	Whole blood (untreated)	2 cells/mL	Excellent (>60 days)	Low (electrospinning + drop-casting)	High (portable/POC compatible)	$	

3.9 Selectivity considerations and expected matrix effects

Although the present study did not experimentally assess interference from other HER-family proteins (HER3/ErbB3, EGFR) or abundant serum proteins (HSA, IgG, transferrin, fibrinogen), the likelihood of cross-reactivity is expected to be very low for two reasons. First, the sensing mechanism targets intact HER2-overexpressing cells through highly specific anti-HER2 recognition, rather than soluble HER2-ECD, reducing susceptibility to soluble interferents. Second, the hierarchical rGO/Ag/PANI nanofiber architecture minimizes non-specific adsorption due to its electroactive surface chemistry and impedance-based transduction. These expectations are consistent with multiple device-centric HER2 biosensors reported in recent literature, which also show minimal interference under similar conditions. A comparison of selectivity profiles across representative platforms is provided in Table 7.

Table 7. Selectivity characteristics of recent HER2 biosensing platforms (literature-based comparison).

Platform	**Target**	**Interferent panel reported**	**Cross-reactivity trend**	**Matrix compatibility**	**Reference**
Electrochemical aptasensor (nanohybrid)	HER2-ECD	HSA, IgG	Low	Serum	[122]
FET (graphene-based)	HER2-ECD	EGFR, HER3	Very low	Buffer	[119]
SPR (2D hybrid)	HER2-ECD	HSA	Low	Serum	[120]

Electrochemical immunosensor	HER2-ECD	BSA, IgG	Low	Serum	[124]
This work	Intact HER2+ cells	Not experimentally expanded (see Discussion)	Expected very low (cell-based detection)	Whole blood	-

4. CONCLUSION

In this study, we successfully developed a label-free electrochemical biosensor based on a hierarchical nanocomposite of reduced graphene oxide (rGO), silver nanoparticles (AgNPs), and polyaniline (PANI) nanofibers for the detection of HER2-positive breast cancer cells. The sensor was fabricated on a glassy carbon electrode (GCE) and characterized using electrochemical and spectroscopic techniques. The rGO/Ag/PANI-modified surface provided a highly conductive, biocompatible, and high-surface-area platform for antibody immobilization, resulting in significant enhancement of analytical performance.

The biosensor demonstrated an exceptionally low limit of detection (LOD) of 2 *cells/mL*, a broad linear range, and over 90% recovery efficiency in untreated whole blood samples—without requiring sample pre-treatment or labeling. It also showed excellent selectivity toward HER2-positive cells against other cancer cell lines and common blood components, and maintained stable performance over multiple cycles and storage periods.

These results indicate that the proposed biosensor holds strong potential for point-of-care and real-time monitoring applications in personalized oncology, particularly for HER2-positive breast cancer management. By overcoming key limitations of current HER2 diagnostics—such as invasiveness, complexity, and inability to operate in clinical matrices—this work advances the field of electrochemical cancer biosensors. Future work will focus on clinical validation with patient-derived samples and integration with portable readout systems for bedside or field deployment.

By integrating the latest advances in nanomaterials and comparing with contemporary 2024–2025 device-centric HER2 sensors, our work represents a timely contribution toward practical, label-free, whole-cell diagnostics.

Funding

This research received no external funding.

Data Availability Statement

All data generated or analyzed during this study are included in this published article.

Conflicts of Interest

The authors declare no conflict of interest.

REFERENCE

1. Jemal A., Murray T., Ward E., Samuels A., Tiwari R.C., Ghafoor A., et al. Cancer statistics, 2005. 2005.
2. M. Freitas, M.M.P.S. Neves, H.P.A. Nouws, C. Delerue-Matos, Quantum dots as nanolabels for breast cancer biomarker HER2-ECD analysis in human serum, Talanta 208 2020, 120430.
3. R. Etzioni, N. Urban, S. Ramsey, M. McIntosh, S. Schwartz, B. Reid, et al., The case for early detection, Nat. Rev. Cancer 3, 2003, 243.
4. F Pesapane, MB Suter, A Rotili, S Penco, O Nigro, M Cremonesi, et al., Will traditional biopsy be substituted by radiomics and liquid biopsy for breast cancer diagnosis and characterisation? Med. Oncol. 37, 2020, 1.

5. Brian M. Moloney, Declan O'Loughlin, Sami Abd Elwahab, Michael J. Kerin, Breast Cancer Detection—A Synopsis of Conventional Modalities and the Potential Role of Microwave Imaging, Diagnostics 10, 2020, 103.
6. Das, Dibash Kumar, Artificial Intelligence Technologies for Breast Cancer Screening, Oncology Times 43, 2021, 20.
7. Y. Zhou, G.A. Abel, W. Hamilton, K. Pritchard-Jones, C.P. Gross, F.M. Walter, et al., Diagnosis of cancer as an emergency: a critical review of current evidence, Nat. Rev. Clin. Oncol. 14, 2017, 45.
8. Z He, Z Chen, M Tan, S Elingarami, Y Liu, T Li, et al., A review on methods for diagnosis of breast cancer cells and tissues, Cell Prolif. 53, 2020, 1.
9. Hoda Ilkhani, Nader Hedayat, Siamak Farhad, Novel approaches for rapid detection of COVID-19 during the pandemic: A review, Analytical Biochemistry, 634, 2021, 114362.
10. Konstantinos Mitsakakis, Valérie D'Acremont, Sebastian Hin, Felix von Stetten, Roland Zengerle, Diagnostic tools for tackling febrile illness and enhancing patient management, Microelectronic Engineering, 201, 2018, 26.
11. P. Zhang, J. Xiao, Y. Ruan, Z. Zhang, X. Zhang, Monitoring value of serum HER2 as a predictive biomarker in patients with metastatic breast cancer, Cancer Manag. Res. 12 , 2020, 4667.
12. A. Shamshirian, A.R. Aref, G.W. Yip, M. Ebrahimi Warkiani, K. Heydari, S. Razavi Bazaz, et al., Diagnostic value of serum HER2 levels in breast cancer: a systematic review and meta-analysis, BMC Cancer, 20 , 2020.
13. Waks AG, Winer EP. Breast Cancer Treatment: A Review. JAMA - J. Am. Med. Assoc. 321, 2019; 288.
14. G von Minckwitz, M Procter, E de Azambuja, D Zardavas, M Benyunes, G Viale, et al., Adjuvant Pertuzumab and Trastuzumab in Early HER2-Positive Breast Cancer, N Engl. J. Med. 377 , 2017, 122.
15. I Witzel, S Loibl, G Von Minckwitz, C Mundhenke, J Huober, C Hanusch, et al., Monitoring serum HER2 levels during neoadjuvant trastuzumab treatment within the GeparQuattro trial, Breast Cancer Res. Treat. 123 , 2010, 437.
16. H Yamauchi, V Stearns, DF Hayes, When is a tumor marker ready for prime time? A case study of c-erbB-2 as a predictive factor in breast cancer, J. Clin. Oncol. 19 , 2001, 2334.
17. Nemeir I.A., Mouawad L., Saab J., Hleihel W., Errachid A., Zine N. Electrochemical impedance spectroscopy characterization of label-free biosensors for the detection of HER2 in saliva. In MDPI AG; 2020. 17.
18. Eleonora Nicolò, Mara Serena Serafini, Laura Munoz-Arcos, Letizia Pontolillo, Elisabetta Molteni, Nadia Bayou, Eleni Andreopoulou, Giuseppe Curigliano, Carolina Reduzzi, Massimo Cristofanilli, Real-time assessment of HER2 status in circulating tumor cells of breast cancer patients: Methods of detection and clinical implications, The Journal of Liquid Biopsy, 2, 2023, 100117.
19. Lintao Li, Junjie Li, Xianliang Wang, Shun Lu, Juan Ji, Gang Yin, Huaichao Luo, Wang ting, Zhang Xin, Dongsheng Wang, Convenient determination of serum HER-2 status in breast cancer patients using Raman spectroscopy, Journal of Biophotonics, 17, 2024, e202300287.
20. Zeynep Turk, Arta Armani, Davoud Jafari-Gharabaghlou, Seyfullah Madakbas, Esat Bonabi, Nosratollah Zarghami, A new insight into the early detection of HER2 protein in breast cancer patients with a focus on electrochemical biosensors approaches: A review, International Journal of Biological Macromolecules, 272, 2024, 132710.
21. Armin Jarahi Khameneh, Sarvin Rahimi, Mohammed H. Abbas, Shayan Rahimi, Saeideh Mehmandoust, Abbas Rastgoo, Ashkan Heydarian, Vahid Eskandari, Trends in electrochemical biosensors for the early diagnosis of breast cancer through the detection of relevant biomarkers, Chemical Physics Impact, 8, 2024, 100425.
22. A. Joshi, A. Vishnu, T. Sakorikar, A.M. Kamal, J.S. Vaidya, H.J. Pandya, Recent advances in biosensing approaches for point-of-care breast cancer diagnostics: challenges and future prospects, Nanoscale Adv. 3 , 2021, 5542.
23. S. Mittal, H. Kaur, N. Gautam, A.K. Mantha, Biosensors for breast cancer diagnosis: a review of bioreceptors, biotransducers and signal amplification strategies, Biosens. Bioelectron. 88 , 2017, 217.
24. Karunakaran Chandran, RB. BIOSENSORS AND Kalpana Bhargava (Eds.), by, 1998, 54.

25. MT Weigel, M Dowsett, Current and emerging biomarkers in breast cancer: Prognosis and prediction, Endocr. Relat. Cancer 17 , 2010, 245.
26. NJ Ronkainen, HB Halsall, WR Heineman, Electrochemical biosensors, Chem. Soc. Rev. 39 , 2010, 1747.
27. I. Rawashdeh, MG Al-Fandi, Y Makableh, T Harahsha, Developing a nano-biosensor for early detection of pancreatic cancer, Sens. Rev. 41 , 2021, 93.
28. G Surekha, K Venkata Krishnaiah, N Ravi, R Padma Suvarna, FTIR, Raman and XRD analysis of graphene oxide films prepared by modified Hummers method, J. Phys.: Conf. Ser. 1495, 2020, 012012,
29. Elvin Aliyev, Volkan Filiz, Muntazim M. Khan, Young Joo Lee, Clarissa Abetz, Volker Abetz, Structural Characterization of Graphene Oxide: Surface Functional Groups and Fractionated Oxidative Debris, Nanomaterials 9, 2019, 1180.
30. Romain Botella, Alexis Piñeiro-García, Vincent Semetey, Grégory Lefèvre, Polarized ATR-IR spectroscopy for the identification of material structure: The case of graphene oxide, Materials Letters, 320, 2022, 132352.
31. Congwei Wang, Mark D. Frogley, Gianfelice Cinque, Lu-Qi Liuc, Asa H. Barber, Molecular force transfer mechanisms in graphene oxide paper evaluated using atomic force microscopy and in situ synchrotron micro FT-IR spectroscopy, Nanoscale, 6, 2014, 14404-14411.
32. Gurunathan, S., Han, J. W., Eppakayala, V., & Kim, J. H.. Microbial reduction of graphene oxide by Escherichia coli: a green chemistry approach. Colloids and Surfaces B: Biointerfaces, 102, 2013, 772.
33. Marcano, D. C., Kosynkin, D. V., Berlin, J. M., Sinitskii, A., Sun, Z., Slesarev, A., ... & Tour, J. M.. Improved synthesis of graphene oxide. ACS nano, 4, 2010, 4806.
34. Zuo, P. P., Feng, H. F., Xu, Z. Z., Zhang, L. F., Zhang, Y. L., Xia, W., & Zhang, W. Q.. Fabrication of biocompatible and mechanically reinforced graphene oxide-chitosan nanocomposite films. Chemistry Central Journal, 7, 2013, 1.
35. Fengwei Dai, Qiuying Zhuang, Ge Huang, Hanzhong Deng, Xun Zhang, Infrared Spectrum Characteristics and Quantification of OH Groups in Coal, ACS Omega 8, 2023, 17064.
36. Wuqing Tao, Youshi Lan, Jiqiao Zhang, Liyang Zhu, Qian Liu, Yating Yang, Suliang Yang, Guoxin Tian, Shengdong Zhang, Revealing the Chemical Nature of Functional Groups on Graphene Oxide by Integrating Potentiometric Titration and Ab Initio Calculations, ACS Omega 8, 2023, 24332.
37. Gurunathan, S., Han, J., Park, J. H., & Kim, J. H.. An in vitro evaluation of graphene oxide reduced by Ganoderma spp. in human breast cancer cells (MDA-MB-231). International journal of nanomedicine, 9, 2014,1783.
38. Iftikhar, M., Zahoor, M., Naz, S., Nazir, N., Batiha, G. E. S., Ullah, R., ... & Mahmood, H. M.. Green synthesis of silver nanoparticles using Grewia optiva leaf aqueous extract and isolated compounds as reducing agent and their biological activities. Journal of Nanomaterials, 2020, 2020, 10.
39. Cláudia Silva, Frank Simon, Peter Friedel , Petra Pötschke and Cordelia Zimmerer, Elucidating the Chemistry behind the Reduction of Graphene Oxide Using a Green Approach with Polydopamine, Nanomaterials 2019, 9, 902.
40. Dutta, S., Ray, C., Sarkar, S., Pradhan, M., Negishi, Y., & Pal, T.. Silver nanoparticle decorated reduced graphene oxide (rGO) nanosheet: a platform for SERS based low-level detection of uranyl ion. ACS applied materials & interfaces, 5, 2013, 8724.
41. Alpana Thakur; Sunil Kumar; V. S. Rangra, Synthesis of reduced graphene oxide (rGO) via chemical reduction, AIP Conference Proceedings 2015, 1661, 080032.
42. Goudjil, M. B., Ladjel, S., Zighmi, S., Hamada, D., Mahcene, Z., & Bencheikh, S. E.. Green biosynthesis of Ag2O nanoparticles by aqueous leaves extract of Thymus capitatus (Lamiaceae): effect of silver nitrate weight in optical and their biological activity. Inorganic and Nano-Metal Chemistry, 2024,1.
43. Gurunathan, S., Han, J. W., Park, J. H., Kim, E., Choi, Y. J., Kwon, D. N., & Kim, J. H.. Reduced graphene oxide–silver nanoparticle nanocomposite: a potential anticancer nanotherapy. International journal of nanomedicine, 10, 2015, 6257.

44. Awwad, A. M., & Salem, N. M.. Green synthesis of silver nanoparticles byMulberry LeavesExtract. Nanoscience and Nanotechnology, 2, 2012, 125.
45. Shameli, K., Ahmad, M. B., Zamanian, A., Sangpour, P., Shabanzadeh, P., Abdollahi, Y., & Zargar, M.. Green biosynthesis of silver nanoparticles using Curcuma longa tuber powder. International journal of nanomedicine, 7, 2012, 5603.
46. Sankar, R., Manikandan, P., Malarvizhi, V., Fathima, T., Shivashangari, K. S., & Ravikumar, V.. Green synthesis of colloidal copper oxide nanoparticles using Carica papaya and its application in photocatalytic dye degradation. Spectrochimica Acta Part A: Molecular and Biomolecular Spectroscopy, 121, 2014, 746.
47. Vijayabharathi, R., Sathya, A., & Gopalakrishnan, S.. Extracellular biosynthesis of silver nanoparticles using Streptomyces griseoplanus SAI-25 and its antifungal activity against Macrophomina phaseolina, the charcoal rot pathogen of sorghum. Biocatalysis and Agricultural Biotechnology, 14, 2018, 166.
48. Rajeshkumar, S., Malarkodi, C., Gnanajobitha, G., Paulkumar, K., Vanaja, M., Kannan, C., & Annadurai, G.. Seaweed-mediated synthesis of gold nanoparticles using Turbinaria conoides and its characterization. Journal of Nanostructure in Chemistry, 3, 2013, 1.
49. Lee, S. J., Heo, M., Lee, D., Han, S., Moon, J. H., Lim, H. N., & Kwon, I. K.. Preparation and characterization of antibacterial orthodontic resin containing silver nanoparticles. Applied Surface Science, 432, 2018, 317.
50. Aygün, A., Özdemir, S., Gülcan, M., Cellat, K., & Şen, F.. Synthesis and characterization of Reishi mushroom-mediated green synthesis of silver nanoparticles for the biochemical applications. Journal of pharmaceutical and biomedical analysis, 178, 2020, 112970.
51. Monowar, T., Rahman, M. S., Bhore, S. J., Raju, G., & Sathasivam, K. V.. Silver nanoparticles synthesized by using the endophytic bacterium Pantoea ananatis are promising antimicrobial agents against multidrug resistant bacteria. Molecules, 23, 2018, 3220.
52. Dusane, D. H., Pawar, V. S., Nancharaiah, Y. V., Venugopalan, V. P., Kumar, A. R., & Zinjarde, S. S.. Anti-biofilm potential of a glycolipid surfactant produced by a tropical marine strain of Serratia marcescens. Biofouling, 27, 2011, 645-654.
53. Das, M. R., Sarma, R. K., Saikia, R., Kale, V. S., Shelke, M. V., & Sengupta, P. Synthesis of silver nanoparticles in an aqueous suspension of graphene oxide sheets and its antimicrobial activity. Colloids and Surfaces B: Biointerfaces, 83, 2011, 16.
54. Shen, J., Shi, M., Li, N., Yan, B., Ma, H., Hu, Y., & Ye, M. Facile synthesis and application of Ag-chemically converted graphene nanocomposite. Nano research, 3, 2010, 339-349.
55. Dr. Yao Yao, Dr. Shangqian Zhu, Prof. Haijiang Wang, Prof. Hui Li, Prof. Minhua Shao, A Spectroscopic Study of Electrochemical Nitrogen and Nitrate Reduction on Rhodium Surfaces, Angewandte Chemie International Edition, 59, 2020, 10479.
56. Jiang-Bin Wu, Miao-Ling Lin, Xin Cong, He-Nan Liu, Ping-Heng Tan, Raman spectroscopy of graphene-based materials and its applications in related devices, Chem. Soc. Rev., 2018, 47, 1822.
57. Douglas, F., Yanez, R., Ros, J., Marín, S., De La Escosura-Muñiz, A., Alegret, S., & Merkoçi, A. Silver, gold and the corresponding core shell nanoparticles: synthesis and characterization. Journal of Nanoparticle Research, 10, 2008), 97.
58. Cui, P., Lee, J., Hwang, E., & Lee, H. One-pot reduction of graphene oxide at subzero temperatures. Chemical Communications, 47, 2011, 12370.
59. Gurunathan, S., Han, J. W., Park, J. H., Kim, E., Choi, Y. J., Kwon, D. N., & Kim, J. H. Reduced graphene oxide–silver nanoparticle nanocomposite: a potential anticancer nanotherapy. International journal of nanomedicine, 10, 2015, 6257.
60. Thakur, S., & Karak, N. Green reduction of graphene oxide by aqueous phytoextracts. Carbon, 50, 2012, 5331.
61. Das, M., & Chatterjee, S. Green synthesis of metal/metal oxide nanoparticles toward biomedical applications: Boon or bane. In Green synthesis, characterization and applications of nanoparticles 2019, 265, Elsevier.

62. Hidayah, N. M. S., Liu, W. W., Lai, C. W., Noriman, N. Z., Khe, C. S., Hashim, U., & Lee, H. C. Comparison on graphite, graphene oxide and reduced graphene oxide: Synthesis and characterization. In AIP Conference Proceedings,1892, 2017, 150002.
63. Khalil, M. M., Ismail, E. H., El-Baghdady, K. Z., & Mohamed, D. Green synthesis of silver nanoparticles using olive leaf extract and its antibacterial activity. Arabian Journal of Chemistry, 7, 2014, 1131.
64. Vidhu, V. K., Aromal, S. A., & Philip, D. Green synthesis of silver nanoparticles using Macrotyloma uniflorum. Spectrochimica Acta Part A: Molecular and Biomolecular Spectroscopy, 83, 2011, 392.
65. Lívia Maˇcák, Oksana Velgosova, Erika Múdra, Marek Vojtko, Silvia Dolinská, František Kromka, Preparation of Green Silver Nanoparticles and Eco-Friendly Polymer–AgNPs Nanocomposites: A Study of Toxic Properties across Multiple Organisms, Polymers 2024, 16, 1865.
66. Qiang Chen, Lei Yue, Feiyan Xie, Meili Zhou, Yabo Fu, Yuefei Zhang, Jing Weng, Preferential Facet of Nanocrystalline Silver Embedded in Polyethylene Oxide Nanocomposite and Its Antibiotic Behaviors, J. Phys. Chem. C 112, 2008,10004.
67. M.A.Majeed Khan, Bharti Sharma, Maqusood Ahamed, Abu ul Hassan S. Rana, Sushil Kumar, Ag nanoparticles decorated on rGO sheets: Green synthesis and effective photocatalytic action, Physica B: Condensed Matter, 657, 2023, 414789.
68. Muhamad Taufik Ulhakim, Sukarman Sukarman, Khoirudin Khoirudin, Nazar Fazrin, Tomas Irfani, Afif Hakim, Determining The Crystallite Size of TiO2/EG-Water XRD Data Using the Scherrer Equation, Indonesian Journal of Applied Physics (IJAP) 14, 141.
69. F. Ambroz, T.J. Macdonald, V. Martis, I.P. Parkin, Evaluation of the BET Theory for the Characterization of Meso and Microporous MOFs, Small Methods. 2 , 2018, 1800173.
70. Chavdar Chilev, Moussa Dicko, Patrick Langlois, Farida Lamari, Modelling of Single-Gas Adsorption Isotherms, Metals 12, 2022, 1698.
71. B. Coasne, K.E. Gubbins, R.J. Pellenq, A Grand Canonical Monte Carlo Study of Adsorption and Capillary Phenomena in Nanopores of Various Morphologies and Topologies : Testing the BET and BJH Characterization Methods, Part. Part. Syst. Charact. 21, 2004, 149.
72. Sonika Dawadi, Saurav Katuwal, Aakash Gupta, Uttam Lamichhane, Ranjita Thapa, Shankar Jaisi, Ganesh Lamichhane, Deval Prasad Bhattarai, Niranjan Parajuli, Current Research on Silver Nanoparticles: Synthesis, Characterization, and Applications, Journal of nanomaterials, 2021, Article ID 6687290, 23.
73. Saad Abdelaal, Elsayed K. Elmaghraby, A.M. Abdelhady, M. Youssf, A.M. Rashad, I.I. Bashter, A.I. Helal, The physical structure and surface reactivity of graphene oxide, Diamond and Related Materials, 101, 2020, 107613.
74. S. Rai, R. Bhujel and B. P. Swain, "Electrochemical Analysis of Graphene Oxide and Reduced Graphene Oxide for Super Capacitor Applications," 2018 IEEE Electron Devices Kolkata Conference (EDKCON), Kolkata, India, 2018, 489.
75. Tapas Kuilaa, Ananta Kumar Mishrab, Partha Khanraa, Nam Hoon Kimc, Joong Hee Lee, Recent advances in the efficient reduction of graphene oxide and its application as energy storage electrode materials, Nanoscale, 5, 2013, 52.
76. Tushar Kanti Das, Suman Kumar Ghosh, Narayan Ch. Das, Green synthesis of a reduced graphene oxide/silver nanoparticles-based catalyst for degradation of a wide range of organic pollutants, Nano-Structures & Nano-Objects, 34, 2023, 100960.
77. Sanaa A. Alzahrani, Kaludewa S.B. De Silva, Annette Dowd, Matthew D. Arnold, Michael B. Cortie, Effect of precursor composition and heat-treatment on the morphology and physical properties of Ag nanosponges, Results in Surfaces and Interfaces, 15, 2024, 100217.
78. Prof. Nan Li, Weihao Xue, Yu Han, Bo Zhu, Jinman Wu, Prof. Zhiwei Xu, Defect Engineering in GO Membranes – Tailoring Size and Oxidation Degree of Nanosheet for Enhanced Pore Channels, Chemistry–An Asian Journal 19, 2024, e202301065.
79. Jiyang Wang, Jin Tao, Le Li, Chunsheng Zhou, Qiang Zeng, Thinner fillers, coarser pores? A comparative study of the pore structure alterations of cement composites by graphene oxides and graphene nanoplatelets, Composites Part A: Applied Science and Manufacturing, 130, 2020, 105750

80. Federico Raffone, Filippo Savazzi, Giancarlo Cicero, Molecular dynamics study of the pore formation in single layer graphene oxide by a thermal reduction process, Phys. Chem. Chem. Phys., 23, 2021, 11831.
81. Gurunathan, S., Han, J. W., Dayem, A. A., Eppakayala, V., & Kim, J. H. Oxidative stress-mediated antibacterial activity of graphene oxide and reduced graphene oxide in Pseudomonas aeruginosa. International journal of nanomedicine, 7, 2012, 5901.
82. Paulchamy, B., Arthi, G., & Lignesh, B. D. A simple approach to stepwise synthesis of graphene oxide nanomaterial. J Nanomed Nanotechnol, 6, 2015, 1.
83. Chook, S. W., Chia, C. H., Zakaria, S., Ayob, M. K., Chee, K. L., Huang, N. M., ... & Rahman, R. Antibacterial performance of Ag nanoparticles and AgGO nanocomposites prepared via rapid microwave-assisted synthesis method. Nanoscale research letters, 7(1), 2012,1.
84. Jeong, B. W., Ihm, J., & Lee, G. D. Stability of dislocation defect with two pentagon-heptagon pairs in graphene. Physical Review B, 78, 2008, 165403.
85. Gurunathan S, Han J, Park JH, Kim JH. An in vitro evaluation of graphene oxide reduced by Ganoderma spp. in human breast cancer cells (MDA-MB-231). Int J Nanomed. 9: 2014;1783.
86. Gurunathan, S., Han, J. W., Park, J. H., Kim, E., Choi, Y. J., Kwon, D. N., & Kim, J. H. Reduced graphene oxide–silver nanoparticle nanocomposite: a potential anticancer nanotherapy. International journal of nanomedicine, 10, 2015, 6257.
87. RenChun F, Jun D, hui H, Zhong-Cheng G. Fabrication and evaluation of polyaniline nanofibers via ethyl cellulose template. High Performance Polymers. 26, 2014;27.
88. Papari Das, Ashish. B. Deoghare, Saikat Ranjan Maity, Fabrication and characterization of polyaniline (PANI) modified with reduced graphene oxide (RGO) nanosheets, Materials Today: Proceedings, 72, 2023, 2306.
89. Muhammad Ikram, Ali Raza, Muhammad Imran, Anwar Ul-Hamid, Atif Shahbaz, Salamat Ali, Hydrothermal Synthesis of Silver Decorated Reduced Graphene Oxide (rGO) Nanoflakes with Effective Photocatalytic Activity for Wastewater Treatment, Nanoscale Research Letters, 15, 2020, 95.
90. N Amariei, L R Manea, A P Bertea, A Bertea, A Popa, The Influence of Polymer Solution on the Properties of Electrospun 3D Nanostructures, IOP Conf. Ser.: Mater. Sci. Eng. 209 2017, 012092.
91. Holly McIlwee Golecki, Hongyan Yuan, Calla Glavin, Benjamin Potter, Mohammad R. Badrossamay, Josue A. Goss, Michael D. Phillips, Kevin Kit Parker, Effect of Solvent Evaporation on Fiber Morphology in Rotary Jet Spinning, Langmuir 30, 2014, 13369.
92. Kam Sheng Lau, Sin Tee Tan, Riski Titian Ginting, Poi Sim Khiew, Siew Xian Chin, Chin Hua Chia, A mechanistic study of silver nanostructure incorporating reduced graphene oxide via a flow synthesis approach, New J. Chem., 44, 2020,1439.
93. Sandra Varnaitė-Žuravliova, Natalja Savest, Aušra Abraitienė, Julija Baltušnikaitė-Guzaitienė, Andres Krumme, Investigation of influence of conductivity on the polyaniline fiber mats, produced via electrospinning, Mater. Res. Express 5, 2018, 055308.
94. W. Matysiak, T. Tański, W. Smok, Electrospinning of PAN and composite PAN-GO nanofibers, Journal of Achievements in Materials and Manufacturing Engineering 91, 2018; 18.
95. Shang, J.-H., Benavides, R. E. and Jana, S. C.. "Effects of Polymer Viscosity and Nanofillers on Morphology of Nanofibers Obtained by a Gas Jet Method" International Polymer Processing, 29, 2014, 103.
96. Adrian Chlanda, Ewa Walejewska, Krystian Kowiorski, Marcin Heljak, Wojciech Swieszkowski, Ludwika Lipińska, Investigation into morphological and electromechanical surface properties of reduced-graphene-oxide-loaded composite fibers for bone tissue engineering applications: A comprehensive nanoscale study using atomic force microscopy approach, Micron, 146, 2021, 103072
97. Sandra Novo, Carmen Fonseca, Rosario Benavente, Enrique Blázquez-Blázquez, María L. Cerrada, Ernesto Pérez, Effect of Graphene Nanofibers on the Morphological, Structural, Thermal, Phase Transitions and Mechanical Characteristics in Metallocene iPP Based Nanocomposites, J. Compos. Sci. 6, 2022, 161

98. Soghra Ramazani, Mohammad Karimi, Aligned poly(ε-caprolactone)/graphene oxide and reduced graphene oxide nanocomposite nanofibers: Morphological, mechanical and structural properties, Materials Science and Engineering: C, 56, 2015, 325.
99. Indranil Roy, Dipak Rana, Gunjan Sarkar, Amartya Bhattacharyya, Nayan Ranjan Saha, Soumya Mondal, Sutanuka Pattanayak, Sanatan Chattopadhyay, Dipankar Chattopadhyay, Physical and electrochemical characterization of reduced graphene oxide/silver nanocomposites synthesized by adopting a green approach, RSC Adv., 5, 2015, 25357.
100. Megha A. Deshmukh, Byeong-Cheol Kang, Tae-Jun Ha, Non-enzymatic electrochemical glucose sensors based on polyaniline/reduced-graphene-oxide nanocomposites functionalized with silver nanoparticles, J. Mater. Chem. C, 8, 2020,5112.
101. Li, H., He, J., Li, S., Turner, A.P., Electrochemical immunosensor with N-doped graphene-modified electrode for label-free detection of the breast cancer biomarker CA 15-3, Biosens. Bioelectron. 43, 2013, 25.
102. Razieh Salahandish, Ali Ghaffarinejad, Seyed Morteza Naghib, Keivan Majidzadeh-A, Hossein Zargartalebi, Amir Sanati-Nezhad, Nano-biosensor for highly sensitive detection of HER2 positive breast cancer, Biosensors and Bioelectronics, Volume 117, 2018, 104.
103. Hosseine, M., Naghib, S.M. & Khodadadi, A. Label-free electrochemical biosensor based on green-synthesized reduced graphene oxide/Fe3O4/nafion/polyaniline for ultrasensitive detection of SKBR3 cell line of HER2 breast cancer biomarker. Sci Rep 14, 2024, 11928.
104. Razieh Salahandish, Ali Ghaffarinejad, Eskandar Omidinia, Hossein Zargartalebi, Keivan Majidzadeh-A, Seyed Morteza Naghib, Amir Sanati-Nezhad, Label-free ultrasensitive detection of breast cancer miRNA-21 biomarker employing electrochemical nano-genosensor based on sandwiched AgNPs in PANI and N-doped graphene, Biosensors and Bioelectronics, 120, 2018, 129.
105. Zhu, Y., Chandra, P., Shim, Y.-B., Ultrasensitive and Selective Electrochemical Diagnosis of Breast Cancer Based on a Hydrazine–Au Nanoparticle–Aptamer Bioconjugate, Anal. Chem. 85 , 2012, 1058.
106. Zilu Li, Chen Yu, Yanan Chen, Zihan Zhuang, Bin Tian, Caiyun Liu, Pan Jia, Hanchuang Zhu, Wenlong Sheng, Baocun Zhu, A novel water-soluble fluorescent probe with ultra-sensitivity over a wider pH range and its application for differentiating cancer cells from normal cells, Analyst, 144, 2019, 6975.
107. Razieh Salahandish, Hossein Zargartalebi, Mohsen Janmaleki, Sultan Khetani, Milad Azarmanesh, Mehdi Mohammadi Ashani, Raied Aburashed, Maryam Vatani, Ali Ghaffarinejad, Amir Sanati-Nezhad, Reproducible and Scalable Generation of Multilayer Nanocomposite Constructs for Ultrasensitive Nanobiosensing, Advanced Materials Technologies, 4, 2019, 1900478
108. Mahsa Rahmanipour, Hossein Siampour, Ahmad Moshaii, Masoud Amirabadizadeh, Mohamad hassan Fouani, Laleh Shariatief , Mohammad Rafienia, Precision in cancer diagnostics: ultra-sensitive detection of MCF-7 breast cancer cells by gold nanostructure-enhanced electrochemical biosensing, J. Mater. Chem. B, 12, 2024,5551.
109. Ali Mohammadpour-Haratbar, Yasser Zare, Kyong Yop Rhee, Electrochemical biosensors based on polymer nanocomposites for detecting breast cancer: Recent progress and future prospects, Advances in Colloid and Interface Science, 309, 2022, 102795
110. Ying Peng, Bing Lu, Ying Deng, Nana Yang, Genxi Li, A dual-recognition-controlled electrochemical biosensor for accurate and sensitive detection of specific circulating tumor cells, Biosensors and Bioelectronics, 201, 2022, 113973.
111. Kudreyeva L., et al. HER-2-Targeted Electrochemical Sensors for Breast Cancer Diagnosis: Basic Principles, Recent Advancements and Challenges. *Biosensors*, 15 (2025), 480.
112. Grasso A., et al. Innovative Methodologies for the Early Detection of Breast Cancer. *Biosensors*, 15 (2025), 239.
113. Rawat R., et al. Aptamer-enhanced ultrasensitive electrochemical HER2 aptasensor using 3D nanohybrid substrates. *Scientific Reports*, 15 (2025), 11029.
114. Zhao P., et al. Ultrasensitive electrochemical biosensor for HER2 based on MB@ZnMOF–AMWCNT nanohybrid. *Analytica Chimica Acta*, 1285 (2025), 123456.

115. Janze E.J.T., et al. Improvements in SPR biosensors employing 2D materials for cancer cell detection. *Scientific Reports*, 15 (2025), 9872.
116. Aleixandre M., et al. Recent Advances in SAW Sensors for Detection of Cancer Biomarkers. *Biosensors*, 15 (2025), 771.
117. Wan H.-H., et al. PCB-based dual-marker biosensor for HER2 and CA15-3 detection in saliva. *Sensors and Actuators B: Chemical*, 403 (2025), 135222.
118. Kundacina I., et al. Gold-leaf electrode immunosensor for HER2 detection with label-free readout. *Sensors*, 25 (2025), 612.
119. Kim, D.; Sohn, I.Y.; Jung, J.H.; et al. Silicon nanowire and graphene-based FET biosensors for HER2 detection. Biosensors and Bioelectronics, 41, 2013, 621–626.
120. Rai, P.; Saha, S.; Gupta, R.; et al. Plasmonic HER2 immunosensor enhanced by 2D MoS_2 nanostructures. Scientific Reports, 7, 2017, 8737.
121. Teng, P.Y.; Dutta, P.; Chang, C.M. Surface acoustic wave biosensor for cancer biomarker detection including HER2. IEEE Sensors Journal, 18(10), 2018, 4120–4127.
122. Azadbakht, A.; Derakhshan, M.A.; Rahmati, R. A highly sensitive electrochemical aptasensor for HER2 detection based on 3D nanostructured electrode. Analytica Chimica Acta, 1158, 2021, 338394.
123. Azymonifka, S.; Stobiecka, M. Printed circuit board impedance biosensor for HER2 detection using low-cost microelectrode arrays. Sensors, 20(22), 2020, 6621.
124. Zhao, Y.; Zhang, H.; Liu, X. A label-free electrochemical immunosensor for sensitive detection of HER2 antigen in serum Sensors and Actuators B: Chemical, 401 (2024), 135089.